

**Faint Stars in the Ursa Minor Dwarf Spheroidal Galaxy: Implications for the  
Low-Mass Stellar Initial Mass Function at High Redshift<sup>1</sup>**

Rosemary F. G. Wyse

*The Johns Hopkins University<sup>2</sup>, Dept. of Physics and Astronomy, Baltimore, MD 21218*

*and*

*University of St Andrews, School of Physics & Astronomy, Scotland, UK*

*and*

*Oxford University, Astrophysics, Oxford, UK*

wyse@pha.jhu.edu

Gerard Gilmore

*Institute of Astronomy, Madingley Road, Cambridge CB3 0HA, UK*

gil@ast.cam.ac.uk

Mark L. Houdashelt

*The Johns Hopkins University, Dept. of Physics and Astronomy, Baltimore, MD 21218*

mlh@pha.jhu.edu

Sofia Feltzing

*Lund Observatory, Box 43, 221 00 Lund, Sweden*

sofia@astro.lu.se

Leslie Hebb

*The Johns Hopkins University, Dept. of Physics and Astronomy, Baltimore, MD 21218*

leslieh@pha.jhu.edu

John S. Gallagher III

*University of Wisconsin, Dept. of Astronomy, Madison, WI 53706*

jsg@astro.wisc.edu

*and*

Tammy A. Smecker-Hane

*University of California, Dept. of Physics & Astronomy, Irvine, CA 92697*

smecker@carina.ps.uci.edu

## ABSTRACT

The stellar initial mass function at high redshift is an important defining property of the first stellar systems to form and may also play a role in various dark matter problems. We here determine the faint stellar luminosity function in an apparently dark-matter-dominated external galaxy in which the stars formed at high redshift. The Ursa Minor dwarf spheroidal galaxy is a system with a particularly simple stellar population – all of the stars being old and metal-poor – similar to that of a classical halo globular cluster. A direct comparison of the faint luminosity functions of the UMi Sph and of similar metallicity, old globular clusters is equivalent to a comparison of the initial *mass* functions and is presented here, based on deep HST WFPC2 and STIS imaging data. We find that these luminosity functions are indistinguishable, down to a luminosity corresponding to  $\sim 0.3 M_{\odot}$ . Our results show that the low-mass stellar IMF for stars that formed at very high redshift is apparently invariant across environments as diverse as those of an extremely low-surface-brightness, dark-matter-dominated dwarf galaxy and a dark-matter-free, high-density globular cluster within the Milky Way.

*Subject headings:* stars: luminosity function, mass function; cosmology: dark matter; galaxies: Ursa Minor, stellar content, kinematics and dynamics.

## 1. Introduction

As a class, the dwarf spheroidal (dSph) companions of the Milky Way, defined by their extremely low central surface brightnesses and low integrated luminosities (e.g. Gallagher & Wyse 1994), have internal stellar velocity dispersions that are in excess of those expected if these systems are in virial equilibrium, with their gravitational potentials being provided by stars with a mass function similar to that observed in the solar neighbourhood (see Mateo 1998 for a recent review). The most plausible explanation for the internal stellar kinematics of these galaxies is the presence of gravitationally dominant dark matter, concentrated on small length scales, leading to mass-to-light ratios that are a factor of ten to fifty above those of normal old stellar populations. The Draco dSph is clearly dominated by an extended dark matter halo (Kleyna et al. 2001). This dark matter must be cold to be dominant on such small scales ( $\lesssim 1$  kpc; cf. Tremaine & Gunn 1979; Gerhard & Spergel 1992; Kleyna et al. 2001). Could some of the dark matter be baryonic? Low-mass stars have high mass-to-light ratios; indeed stars of mass  $0.3 M_{\odot}$  and metallicity one-hundredth of the solar value – of order the lowest mean metallicity measured for stars in dSph – have V-band mass-to-light ratios of 24 in solar units (Baraffe et al. 1997). Of course faint stars could be viable

---

<sup>1</sup>Based on observations with the NASA/ESA Hubble Space Telescope obtained at the Space Telescope Science Institute, operated by AURA Inc., under NASA contract NAS5-26555. These observations are associated with proposal GO 7419.

<sup>2</sup>Permanent address

dark matter candidates only if the stellar initial mass function (IMF) in these systems were very different from the apparently invariant IMF observed for other stellar systems, such as the solar neighbourhood or globular clusters (cf. Gilmore 2001). In addition to its possible relevance to dark matter problems, the IMF of low-mass stars in a wide variety of astrophysical systems is of considerable intrinsic interest (see e.g. papers in Gilmore & Howell 1998). In particular, the form of the IMF at high redshift is of crucial importance for many aspects of galaxy formation and evolution, such as the understanding of background light measurements (e.g. Madau & Pozzetti 2000) and chemical evolution.

A direct test of the hypothesis that the dark matter in dwarf spheroidal galaxies is in the form of low-mass stars is provided by comparison of the faint stellar luminosity function in a dSph galaxy with that of a stellar system that has similar stellar age and metallicity distributions and which is known to contain no dark matter. Empirical comparison of such luminosity functions minimises the need to use the highly uncertain and metallicity-dependent transformations between mass and light (see D’Antona 1998 for a discussion of this point). Systems with stars only in narrow ranges of age and metallicity allow the most straightforward interpretation.

The stellar population of the Ursa Minor dwarf Spheroidal (UMi dSph) is characterized by narrow distributions of age and of metallicity (e.g. Olszewski & Aaronson 1985; Mighell & Burke 1999; Hernandez, Gilmore & Valls-Gabaud 2000; Carrera et al. 2002), with a dominant component that is similar to that of a classical halo globular cluster such as M92 or M15, i.e. old ( $\gtrsim 12$  Gyr) and metal-poor (mean  $[\text{Fe}/\text{H}] \sim -2$  dex). However, in contrast to globular clusters, which have typical  $(M/L)_V \lesssim 3$  (e.g. Meylan 2001), the internal dynamics of the UMi dSph are apparently dominated by dark matter, since the derived core mass-to-light ratio is  $(M/L)_V \gtrsim 60$ , based on the relatively high value of its internal stellar velocity dispersion (Hargreaves et al. 1994; see review of Mateo 1998). Faint star counts in the Ursa Minor dSph thus allow determination of the low-mass IMF in a dark-matter-dominated external galaxy in which the bulk of the stars formed at high redshift (a lookback time of 12 Gyr, the stellar age, corresponds to a redshift of  $\gtrsim 2.5$  for a ‘concordance’ Lambda-dominated cosmology; e.g. Bahcall et al. 1999).

We thus undertook deep imaging with the Hubble Space Telescope of a field close to the centre of the Ursa Minor dSph. Various relevant properties of this galaxy are collected in Table 1. While having an integrated luminosity similar to that of a globular cluster, the central surface brightness of the Ursa Minor dSph, at only  $\sim 25.5$  V-mag/sq arcsec, with a corresponding central luminosity density of only  $0.006 L_\odot \text{ pc}^{-3}$ , is many orders of magnitude lower than that of a typical globular cluster (e.g. M92 has a central surface brightness of  $\sim 15.6$  V-mag/sq arcsec and a central luminosity density of  $3 \times 10^4 L_\odot \text{ pc}^{-3}$ ; Harris 1996). While most models of dSph evolution invoke some mass loss and expansion (e.g. Dekel & Silk 1986), it is most likely that the dSph never had a central density comparable to that of a globular cluster. Did the stars in these two disparate systems form with the same Initial Mass Function?

## 2. Deep HST Star Counts in the Ursa Minor Dwarf Spheroidal Galaxy

### 2.1. The Approach

We obtained deep, multi-instrument (WFPC2, STIS and NICMOS), images of the central regions of the Ursa Minor dSph galaxy, from which the faint stellar luminosity function was derived. We also obtained comparable data for an off-field, at similar Galactic coordinates, to understand the contamination by non-member stars, unresolved systems such as background galaxies, etc. The derived luminosity functions may be directly compared to those of globular clusters of the same stellar age and metallicity as the dominant population of the UMi dSph. WFPC2 luminosity functions of fields at intermediate radius in metal-poor, old globular clusters are available, as discussed below (it is important that the present-day faint luminosity function be a good measure of the initial faint luminosity function, thus favouring fields at intermediate radius). We obtained NICMOS and STIS imaging data for fields in the globular clusters 47 Tuc and M15 to allow this direct comparison, and to enable empirical calibration of magnitudes measured with the non-standard STIS optical longpass (LP) filter (see Houdashelt, Wyse & Gilmore 2001).

### 2.2. The Experiment

We obtained Hubble Space Telescope deep imaging data of a field near the centre of the Ursa Minor dSph (program GO 7419), using STIS (the primary instrument; CCD + LP filter), WFPC2 (parallel observations; F606W & F814W filters) and NICMOS (parallel observations; NIC1: F140W filter; NIC2: F160W filter; NIC3: out of focus). The STIS pointing is  $3'$  WSW<sup>3</sup> (position angle  $\sim 200^\circ$ ) of the centre of the UMi dSph galaxy, adopting the centre derived by Kleyna et al. (1998) from their ‘deep’ ( $V \lesssim 22$ ) ground-based, wide-area star count data. This field was chosen because of extant archival WFPC2 data (GTO 6282).

At the apparent magnitudes of interest here, the (metal-poor) Ursa Minor stars are sufficiently blue that stars from the Galactic halo will be the main stellar contaminant. Star count models (e.g. Gilmore 1981) and observational data in other high-Galactic latitude lines of sight (e.g. the HDF; Elson, Santiago & Gilmore 1996) predict there will be around 10 Galactic main-sequence stars plus a few old white dwarfs (of uncertain colours; cf. Hansen 1999) in a WFPC2 field of view (FOV) of  $\sim 4.5$  sq arcmin, and proportionally less in the STIS-LP FOV ( $\sim 0.4$  sq arcmin) and in the NIC1 and NIC2 FOVs ( $\lesssim 0.04$  sq arcmin and  $\sim 0.1$  sq arcmin, respectively); unresolved systems, such as background galaxies, or distant globular clusters and star-forming regions, also contribute to the objects detected. Thus to provide an empirical contamination control, similarly exposed data for an offset field at comparable (high) Galactic latitude coordinates to those of the UMi field ( $\ell = 105^\circ$ ,  $b = 45^\circ$ ) were acquired; we selected a field along the minor axis that lies  $\gtrsim 2.5$

---

<sup>3</sup>The Ursa Minor dSph is significantly flattened, with axial ratio of  $\sim 0.6$  (see Kleyna et al. 1998, their Table 1, and also Irwin & Hatzidimitriou 1995). The major axis is NE-SW at position angle  $\sim 50^\circ$ .

(major-axis) tidal radii<sup>4</sup> from the centre of the Ursa Minor dSph. Galactic reddening along these lines of sight is small,  $E(B-V) \lesssim 0.03$  (e.g. Schlegel, Finkbeiner & Davis 1998).

We chose not to implement a standard dithered observing pattern, since this would have greatly compromised the efficiency of the data acquisition with the parallel instruments. Successive failures of HST while attempting our observations resulted in the data for the Ursa Minor dSph field being collected over three years, 1997–1999. The analysis presented here is based on a significantly augmented dataset compared to our earlier published results (Feltzing, Gilmore & Wyse 1999), which analysed the WFPC2 data collected in 1997 only.

We discuss below the data from WFPC2, STIS and NICMOS in turn. The resulting colour-magnitude diagrams and luminosity functions are then derived, and their implications are discussed. All of the data reduction and photometry was performed within the IRAF<sup>5</sup> environment. Our main scientific results are in sections 6–10 and the less dedicated reader may wish to start there.

### 2.3. Comparison Objects

From the ground-based observations of Olszewski & Aaronson (1985) that reached below the main-sequence turnoff of the Ursa Minor dSph, it is clear that the dominant population is old and metal-poor, like that of the globular cluster M92 (NGC 6341). Indeed, Mighell & Burke (1999) carried out a detailed comparison between the WFPC2 colour-magnitude diagram (CMD) of the Ursa Minor dSph (derived from data taken as part of GTO 6282) that reaches  $\sim 2.5$  mag below the main-sequence turnoff and the ground-based CMD of M92 from Johnson & Bolte (1998). These authors found very similar fiducial sequences, once the relative distance modulus had been accounted for, with a colour offset of only 0.01 mag in V–I (after transformation to the Johnson-Cousins system) between the main sequence of the Ursa Minor dSph and that of M92. The RGB of the Ursa Minor dSph was found to be slightly redder than that of M92, but small number statistics makes such a conclusion rather uncertain (see Fig. 13 of Mighell & Burke 1999). These data strengthen the conclusion that the dominant stellar population of the Ursa Minor dSph is similar to that of a classical halo globular cluster.

In order to provide transformation-free data for metal-poor, old stars with which to compare our STIS observations of the Ursa Minor dSph, we also obtained STIS CCD (LP filter) observations of the globular cluster M15 (NGC 7078) in a field with extant WFPC2  $V_{606}$  and  $I_{814}$  data (de Marchi & Paresce 1995; Piotto, Cool & King 1997). We also obtained NIC2 H-band data (F160W filter) for a portion of this M15 field, again to allow a direct comparison of the UMi data with those for a known metal-poor, old population. Houdashelt et al. (2001) present an analysis and discussion of

---

<sup>4</sup>Our offset field, 115' from the centre of the UMi dSph, was at Galactic coordinates of ( $\ell = 107^\circ$ ,  $b = 45^\circ$ ). Irwin & Hatzidimitriou (1995) derive a value of 50' for the major-axis tidal radius of UMi, while Kleyana et al. (1998) derive a value of 39'.

<sup>5</sup>IRAF is distributed by National Optical Astronomy Observatories, operated by the Association of Universities for Research in Astronomy, Inc., under contract with the National Science Foundation.

our STIS and WFPC2 data for M15 and for another globular cluster, 47 Tuc (NGC 104).

### 3. The WFPC2 Data

The WFPC2 fields within the Ursa Minor dSph (hereafter ‘UMi-WFPC2’) and offset from the galaxy (‘UMi-off-WFPC2’) have WFALL coordinates, measured using the METRIC task, of  $(\alpha_{2000}, \delta_{2000}) = (15^h 07^m 50.85^s, +67^\circ 08' 47.93'')$  and  $(\alpha_{2000}, \delta_{2000}) = (14^h 55^m 26.0^s, +68^\circ 35' 42.2'')$ , respectively.

A summary of the observations of these fields is given in Table 2. Note that there are additional images of the UMi-WFPC2 field, compared to the UMi-off-WFPC2 field; some observations of the UMi field were repeated to compensate for initial failures of the primary STIS instrument; the parallel instrument WFPC2, which did not fail, thus obtained extra exposure time in this field.

#### 3.1. Combining WFPC2 images

##### 3.1.1. UMi-WFPC2 field

There were sufficiently large offsets between images of the UMi field taken in successive years that it was beneficial to utilize the drizzling technique when combining the images. The standard drizzling recipe was followed, using the STSDAS DITHER and DRIZZLE packages (see Fruchter & Hook 1997 and the STScI web pages), except when it came to determining the relative shifts between the images taken in the three different observing seasons.

The chips of WFPC2 are known to drift in relative position with an amplitude of around one pixel per year, which complicates the drizzling procedure for datasets, such as the present one, taken over an extended time period (see Fruchter & Mutchler 1998). We implemented the following approach: we first used SHIFTFIND to determine the shifts among each group of images that had been observed in the same year – three groups of V- and I-band images. Then we drizzled each group of images separately to obtain three cosmic-ray-free images for each filter. We carefully measured the positions of several stars on each of these new combined images and determined the average shifts from year to year. These average shifts were then added to the shifts found within each annual subset of images, providing greatly improved final drizzled images. These final images have total exposure times of 14600s in F606W and of 17200s in F814W. The final UMi-WFPC2 V-band image is shown in Fig. 1.

All of the WFPC2 images were initially put through the standard data processing pipeline. Corrections for charge transfer inefficiency were implemented using the formula in Whitmore, Heyer & Casertano (1999). As the data were taken over a time-span of over two years, we adopted an average date to calculate the amplitude of the corrections. The error introduced by this procedure is negligible compared to other uncertainties.

### 3.1.2. UMi-off-WFPC2 field

The data reduction for this field is described in Feltzing, Gilmore & Wyse (1999); there are no further observations to augment that dataset. The images of the UMi-off-WFPC2 field were all obtained in one observing block and were well aligned. We used CRREJ to combine them; the value of the relevant SCALENOISE parameter was determined and applied separately for each WF chip, following the procedure outlined in the CRREJ help file. The total exposure time in each filter for the UMi-off-WFPC2 field was 9600s. The final V-band UMi-off-WFPC2 image is shown in Fig. 2.

## 3.2. WFPC2 Photometry and image classification

### 3.2.1. UMi-WFPC2 Field

Photometry was derived from the drizzled images using the IRAF DAOPHOT package. Aperture photometry was first derived with the PHOT task, using an aperture radius<sup>6</sup> of 2 pixels (our images are uncrowded). The noise in the background varies rapidly over the drizzled image, so a mean estimate of the sky background was used because it proved to be more stable than the usually recommended median.

Since our aim was to go as faint as possible while retaining reliability, we deliberately adopted a low value of the detection threshold. This leads to an inevitably large number of spurious detections at faint magnitudes, which we subsequently removed by requiring that an object be detected and meet the stellar photometric criteria (described below) in both WFPC2 bandpasses. The appropriate detection threshold was identified by running DAOFIND using different values and examining the number of detections as a function of  $n \times \sigma_{\text{bkgrnd}}$ . We adopted a threshold of  $2.5\sigma_{\text{bkgrnd}}$ , which provided 4000–5000 detections on each WF chip.

The drizzling procedure obviously affects the point spread functions (psfs). Thus we created psfs interactively for each filter and WF chip, using several isolated, bright stars per chip, allowing the psf to vary over the image. These psfs were used to obtain psf-fitted photometry, using the aperture photometry as input. The ALLSTAR output includes two statistics,  $\chi$  and sharpness, that may be used to help distinguish valid stars/point sources from other objects, such as background galaxies, etc. We employed cuts in the values of these two statistics, rejecting objects that had values above the thresholds given in Table 3. An illustration of the  $\chi$  and sharpness distributions for WF4 and filter F814W is given in Fig. 3; the quality of the psfs is clearly quite satisfactory.

The psf photometry derived in this way provided a coordinate list that was used to derive new psf-fitted photometry using the scheme described by Cool & King (1996), which provides results optimised for faint objects<sup>7</sup>. The corresponding colour-magnitude diagrams for both aperture

---

<sup>6</sup>The sizes of all photometric apertures are specified here in terms of their radii.

<sup>7</sup>This scheme sets the parameters FLATERR, PROFERR, and CLIPEXP in DAOPARS to zero, basically invoking a simple weighting scheme. With this it is possible to extract high quality photometry at faint magnitudes, fainter than possible with either aperture- or “standard” psf-fitted photometry.

photometry and psf-fitted photometry were constructed by cross-correlating the stellar coordinates in the two filters, using a matching radius of one pixel. A total of 2038, 1751, and 1698 stars were detected in this way on WF2, WF3, and WF4, respectively (note that the variation in the relative numbers of stars in different detectors is most likely dominated by noise statistics rather than any true variation across the face of the Ursa Minor dSph galaxy; we return to this point below in section 8.4).

Calibration of the photometry followed the standard routine outlined in Holtzman et al. (1995) and also described in Feltzing & Gilmore (2000). Aperture corrections (to a  $0.5''$  radius aperture) were derived from bright, isolated stars in each image individually and are listed in Table 3. The scatter in the photometric calibrations is  $\sim 6\%$ , providing a calibration uncertainty which is small compared to the bin sizes that we adopt for our luminosity functions below.

### 3.2.2. *UMi-off-WFPC2 Field*

The procedure used here is described in Feltzing, Gilmore & Wyse (1999), with the psf-photometry  $\chi$  and sharpness selection criteria from the UMi field being applied. The number of stellar objects detected here is approximately the number of field stars expected (see Section 2.2), and their luminosity function is tabulated in Feltzing, Gilmore & Wyse (1999), where all details of the reduction and analysis are given. For completeness, the photometry for the 21 stellar objects detected in this field is given in Table 4 (magnitudes in a  $0.5''$  radius aperture).

## 3.3. WFPC2 Completeness

Completeness, i.e. the percentage of stars at a given magnitude that are detected, has been calculated using standard techniques, i.e. by adding artificial stars to the drizzled images and then rerunning the detection and photometry procedures, described above, on these images. As can be seen from Fig. 1, our UMi-WFPC2 field is rather sparse, and crowding is not an important source of error. For each magnitude bin used in our WFPC2 luminosity functions below, 265 artificial stars were added to the V and I images separately, but with the colour for each artificial star set to match the observed fiducial main sequence of the Ursa Minor dSph (shown in Figs. 20 and 21 below). The retrieved stars were then put through the same selection routine (i.e. the  $\chi$  and sharpness constraints) adopted for the real stars, with the further requirements that the measured magnitude of the retrieved artificial star be within 0.5 mag of the input magnitude and the coordinates of the retrieved star be within one pixel of the input coordinates. Finally, we counted only stars that met all of these criteria in *both* F606W and F814W. This procedure minimises spurious results from bin-jumping, etc. (see also Bellazzini et al. 2002). The derived completeness functions are shown in Figure 4 and tabulated in Tables 5 and 6. The 50% completeness limits for each of the WF chips are (for WF2, WF3, WF4 in turn)  $V_{606,50\%} = 28.35, 28.29, 28.34$  and  $I_{814,50\%} = 27.25, 27.16, 27.12$ . The weighted average of the three WF chips gives a net 50% completeness limit of  $I_{814} = 27.19$  and  $V_{606} = 28.35$ ; this is the limit indicated later in the luminosity function plots. The luminosity

function itself is the sum of the corrected counts in the individual chips, each derived using that chip’s completeness function.

#### 4. The STIS data

Images were taken with the STIS instrument, using the CCD and LP filter, pointed at the previously observed (WFPC2 GTO) field near the centre of the Ursa Minor dSph (hereafter ‘UMi-STIS’) with coordinates  $(\alpha_{2000}, \delta_{2000}) = (15^h 08^m 27.96^s, +67^\circ 12' 41.16'')$ , and at a field 2–3 tidal radii away (hereafter ‘UMi-off-STIS’) with coordinates  $(\alpha_{2000}, \delta_{2000}) = (14^h 56^m 00.0^s, +68^\circ 40' 00.0'')$ . The LP filter provides a rather flat throughput longward of  $\sim 6000 \text{ \AA}$  until the CCD limit at  $\sim 1\mu$ , and we will refer to magnitudes in this filter as  $I_{LP}$ . The conversion of photometric systems (such as transforming the non-standard  $I_{LP}$  to Cousins I) is a function of stellar metallicity, surface gravity (i.e. age), etc. To maximize the reliability of our comparisons of the derived luminosity functions of the UMi dSph with those of globular clusters, we also obtained directly comparable STIS CCD LP data for a globular cluster with stellar population similar to that of the UMi dSph. Thus, we obtained a STIS/LP image of the globular cluster M15, at an intermediate projected radius within the cluster, in a field that had already been studied with WFPC2. The photometric analysis of these globular cluster data (together with those which we also obtained for the more metal-rich globular cluster 47 Tuc, to determine the amplitude of any metallicity effects in the transformations) are presented in Houdashelt et al. (2001). The datasets for the UMi-STIS, UMi-off-STIS and M15 fields are also summarised in Table 2.

The STIS observations were obtained in the ACCUM observing mode with gain = 4. The STIS CCD consists of  $1024 \times 1024$  pixels with a plate scale of  $0.05'' \text{ pixel}^{-1}$ , but use of the LP filter reduces the available field of view to approximately  $28'' \times 50''$ . The UMi-STIS and UMi-off-STIS data were binned on-chip in  $2 \times 2$  pixel bins to give an effective pixel size of  $0.10''$ , similar to that of the WF CCDs, and were obtained with CR-SPLIT = 2; the M15 data were unbinned and obtained with CR-SPLIT = 5. The characteristics of STIS and the on-orbit performance of the instrument are described by Woodgate et al. (1998) and Kimble et al. (1998), respectively.

##### 4.1. Combining the STIS Data

All of the raw STIS images were calibrated using appropriate reference files (darks, flats, etc.) and the IRAF task CALSTIS. The amplitude of any possible effect due to charge-transfer inefficiency is ignorable for our present purposes, and we did not implement any CTI corrections. For the M15 data, this was the only data reduction required. The multiple images of the UMi field were obtained over three years and had small but non-negligible shifts between images taken in different years ( $\Delta x < 2$  pixels and  $\Delta y \lesssim 3$  pixels); these were combined using the DRIZZLE software, following the general procedure described in The Drizzling Cookbook (Gonzaga et al. 1998). For consistency, we also drizzled the UMi-off-STIS images, even though only subpixel shifts were seen in those data. As the UMi-STIS and UMi-off-STIS data are binned, the COEFFS parameter used

in the `BLOT`, `CROSSDRIZ`, and `DRIZZLE` tasks was left blank, i.e. no geometric distortion correction was applied. The image offsets were all sufficiently small that we used `DRIZZLE` simply to perform a basic shift-and-add procedure to combine the images, setting the parameters `PIXFRAC` and `SCALE` to unity in the final drizzling step. The final STIS LP image of M15 is shown in Houdashelt et al. (2001); the drizzled images of the UMi-STIS and UMi-off-STIS fields are shown in Figs. 5 and 6, respectively.

## 4.2. STIS Photometry and Image Classification

The STIS LP photometry was performed using the `DAOPHOT` software within `IRAF`. The photometry of M15 is fully described in Houdashelt et al. (2001).

### 4.2.1. UMi-STIS field

The positions of stars in the images were found using the task `DAOFIND` and adopting a  $3.5\sigma$  detection threshold (this is a higher threshold than adopted for the `WFPC2` data since we have STIS data in only one passband). Aperture magnitudes were then calculated with the `PHOT` task using a 2 pixel aperture; for each star, the sky brightness was estimated from the mode in a circular annulus, centred on the star, having an inner radius of 5 pixels ( $\sim 0.5''$ ) and a width of 5 pixels. To derive the magnitudes in an aperture having a radius of  $0.5''$ , aperture corrections were calculated from 43 bright, isolated stars in the image using the task `MKAPFILE`.

While all of the STIS-LP luminosity functions ultimately presented here are constructed from aperture magnitudes, psf photometry was also performed to provide goodness-of-fit statistics for removing non-stellar detections from the star lists, and to determine the empirical psf for use in the completeness tests. However, the on-chip binning of the UMi-STIS and UMi-off-STIS data was found to introduce complications in the psf photometry, as will be seen below. The (unbinned) M15 data were useful for comparison purposes and will be described here as needed; a full discussion of these data was given in Houdashelt et al. (2001).

The empirical psfs of the M15 and UMi-STIS images were measured in the same manner using, respectively, 40 and 29 bright, isolated stars that were spatially distributed throughout each image. A psf which varied quadratically with position on the STIS CCD was adopted (`DAOPARS.VARORDER = 2`); a penny2 function was found to fit the stellar profiles best in the M15 data, while for the UMi data, a moffat15 function proved superior.

Figs. 7 and 8 show the  $\chi$  and sharpness distributions of the objects detected in the M15 and UMi-STIS LP images, respectively, with the dotted lines in each panel of these figures showing the expected  $\chi$  and sharpness values of stars that are perfectly fit by the empirical PSFs. The M15 data scatter about these optimal  $\chi$  and sharpness values, and the selection criteria that we chose for the M15 stars are  $\chi \leq 1.8$  and  $-0.2 \leq \text{sharpness} \leq 0.2$  (indicated by the dashed lines on the figure; note that since we have data in only one band, unlike the `WFPC2` data, we implement a

lower cut in the sharpness also).

The  $\chi$  distribution of the (binned) UMi-STIS data is unusual, curving to higher  $\chi$  values at faint magnitudes and making it impossible to apply a simple, constant  $\chi$  threshold, as is the normal practice. We experimented with changing the various IRAF DAOPHOT parameter values such as PROFERR and FLATERR, but the general shape of the  $\chi$  distribution remained essentially as shown. We adopted the following criteria for unresolved objects in the UMi-STIS data:  $-0.1 \leq \text{sharpness} \leq 0.2$ ,  $\chi \leq 2.0$  for  $I_{LP} \leq 26.75$ , and  $\chi \leq 1.5 \times I_{LP} - 38.125$  for  $I_{LP} > 26.75$ . These are indicated by the dashed lines in Fig. 8. These criteria were determined empirically by direct examination by eye of the 200 brightest objects detected on the UMi-STIS image. This revealed that all of the objects lying above the dashed line in the top ( $\chi$ ) panel of Figure 8 are either galaxies, point-like sources lying within the halos of galaxies, or stellar blends, and thus should indeed be rejected.

The details of these unusual psf statistics are not fully understood but one can demonstrate that they arose as an artifact of the binning. This is illustrated in Fig. 9, which shows the  $\chi$  and sharpness distributions that result after binning the post-CALSTIS M15 data prior to psf fitting. These distributions are very similar to those shown in Fig. 8, giving us confidence that the adopted selection criteria do correctly select all stellar objects. As a further test, we compared magnitudes for M15 stars derived from both the binned and the unbinned data. Fig. 10 shows that the maximum systematic difference between these magnitude scales is  $\lesssim 0.05$  mag, even at the faintest magnitudes. This shows that reliable and accurate star classification and photometry are being achieved with the binned data.

#### 4.2.2. UMi-off-STIS field

The small (sub-pixel) offsets between images of this field provide poorer removal of cosmic rays within DRIZZLE and makes identification of real stellar images more difficult. There is a further complication in the analysis of this field, as only a single bright star is obvious in the UMi-off-STIS image (see Fig. 6); it alone was used to estimate the aperture correction for any other ‘stars’ in this image. The lack of other bright stars makes it impossible to construct a psf for this image in the usual way, especially one that could include variation with position on the CCD. Thus, we obtained psf photometry of the UMi-off-STIS image in two ways: (1) using the psf derived from the single bright star in this image, and (2) using the psf derived from the final drizzled image of the UMi field. The  $\chi$  and sharpness distributions using these two psfs are shown in Fig. 11. The UMi-STIS psf appears to provide the better object detection, in that the sharpness distribution in particular is more ‘normal’.

However, in contrast with the UMi-off-WFPC2 field discussed above, application of the selection criteria for unresolved objects from the UMi-STIS data results in many detections. It is highly unlikely that either Galactic star counts or counts of unresolved galaxies vary significantly on such a small angular scale as the distance between the WFPC2 and STIS fields. We have determined, by visual examination of the UMi-off-STIS image, that the objects with  $I_{LP} < 28$  in the bottom, right-hand panel of Figure 11 that apparently meet the sharpness criterion for unresolved objects

are in fact instead clearly resolved galaxies. Further, their luminosity distribution matches the bright end of the STIS galaxy counts in the Hubble Deep Field South (Gardner et al. 2000). We obtained similar results with a psf derived from only the subset of the UMi-STIS data that was taken in 1997, the same year that the UMi-off-STIS data were taken; this approach was designed to minimise the effects of possible temporal variation in the psf.

It appears that the UMi-STIS psf is a poor representation of the true UMi-off-STIS psf, even when restricted to data taken close in time to the UMi-off-STIS observations. Given the  $\chi$  and sharpness distributions of Fig. 11, it is clear that, for either the UMi-STIS or UMi-off-STIS psf, we cannot independently estimate the  $\chi$  and sharpness values at which resolved and unresolved objects can be separated in the UMi-off-STIS image.

Using the psf derived from the one bright star in the UMi-off-STIS image and adopting the  $\chi$  and sharpness selection criteria derived from the UMi-STIS image gives objects with the luminosity function shown by the histogram in Fig. 12. These objects are all very faint and are likely to be spurious detections, produced by warm pixels, image defects, etc., that could not be removed during the drizzling process due to the very small (subpixel) offsets among the UMi-off-STIS datasets. There will be fewer such detections in the UMi-STIS field than in the UMi-off-STIS field due to the larger pixel offsets among the individual UMi-STIS images (which span a longer time period than the images of the offset fields). Indeed, the drizzled image of the UMi-STIS field that incorporated only the 1997 datasets revealed many such artifacts which were not seen in the UMi-STIS image constructed from all of the available datasets. Scaling the UMi-off-WFPC2 star counts to the STIS-LP field of view, we would expect only  $\sim 2$  stellar objects in the UMi-off-STIS field, so the luminosity function shown in Fig. 12 is highly likely to be an overestimate of the contamination by unresolved objects in the UMi  $I_{LP}$  luminosity function. Given this uncertainty, we show below the UMi STIS-LP luminosity functions both with and without subtraction of the offset field. One should also bear in mind that the repeated observations have resulted in a longer total exposure time for the UMi-STIS field compared to the UMi-off-STIS field.

### 4.3. STIS Completeness

The completeness functions (CFs) for the M15 data and for the UMi dSph data were determined by adding  $\sim 200$  artificial stars to the respective images, each having the magnitude of the centre of one of the luminosity function bins, and then performing object detection and photometry on the resulting images; the completeness functions are the fractions of artificial stars detected, meeting the psf selection criteria and lying within 0.5 mag of their input magnitudes. The final completeness functions are the averages of 10 iterations of this procedure and are given in column 3 of Table 7 and column 4 of Table 8 for M15 and the UMi dSph galaxy, respectively. To judge whether or not crowding in the UMi-STIS image is affecting the completeness functions (it is not), we performed similar completeness tests on the UMi-off-STIS image using the UMi-STIS psf. Each of these completeness functions is illustrated in Fig. 13. Linearly interpolating the final CFs, the 50% completeness limit of the UMi data is  $I_{LP} = 28.86$ , corresponding to an absolute magnitude of  $M_{LP} \sim 9.7$ , while for M15 it is  $I_{LP} = 26.57$ , corresponding to the fainter absolute magnitude of

$M_{LP} \sim 11.5$ .

As a further investigation of the data, we added  $\sim 800$  artificial stars of various magnitudes to the UMi-STIS image, each star having a magnitude at the centre of a luminosity function bin, with the number at each bin centre chosen from a power-law fit to the observed luminosity function of M15. In Fig. 14, the recovered luminosity function of the artificial stars (solid line) is compared to input (open circles) and to the observed (i.e. not completeness-corrected) luminosity function of the UMi dSph, (asterisks; the values obtained with and without subtraction of the off-field counts from Fig. 12 are connected). This demonstrates that when a power-law luminosity function similar to that of M15 is added to the UMi-STIS image, the returned luminosity function is very similar to the observed luminosity function of the UMi dSph.

#### 4.4. STIS-WFPC2 Colour-Magnitude Diagrams

The UMi-STIS pointing was chosen to overlie a field with extant WFPC2 observations (from GTO 6282, which provided the data analysed by Mighell & Burke 1999). Subsequently, this field was repeated with WFPC2 as part of a program to measure proper motions of galactic satellites (GO 8095; to avoid duplication of science, we will not here consider the derivation of proper motion). Thus, at least for the brighter stars, we can do a cross-check on the reality of the detections.

We extracted the WFPC2 data from the archive and reduced the images using the IRAF task CALWP2. The images were then combined through drizzling, again using the standard techniques described in The Drizzling Cookbook (Gonzaga et al. 1998). Comparing the UMi STIS-LP image with these WFPC2 data, we verified that the ‘non-stellar’ objects rejected from the UMi-STIS photometry database by our adopted selection criteria were either (1) not detected in the WFPC2 frames, or (2) did not lie close to the WFPC2 main-sequence ridge line of the UMi dSph.

These data also allow us to constrain the relationship between  $I_{814}$  and  $I_{LP}$ , the magnitudes in the WFPC2 F814W and STIS LP filters, respectively. Our earlier work analysing the deep data for the globular cluster M15 (Houdashelt et al. 2001) can be used to establish a tight relationship between the two magnitudes, namely

$$M_{814,0} = -0.783(\pm 0.015) + 0.931(\pm 0.002) \times M_{LP,0}. \quad (1)$$

The shallower UMi dSph colour-magnitude data allow us to verify that, over the (limited) absolute magnitude range in common between the M15 and UMi datasets, the Ursa Minor dSph stars obey the same relation between  $I_{LP}$  and  $I_{814}$  as the M15 stars. This is not surprising, given that several groups have established the similarity of the stellar populations over this range.

We will use this relation below to transform our derived  $I_{LP}$  luminosity function for the UMi dSph into an  $I_{814}$  luminosity function and to compare it with our directly observed  $I_{814}$  luminosity function, providing a check on the robustness of our results.

## 5. The NICMOS Data

NICMOS consists of three cameras (NIC1, NIC2 and NIC3), each equipped with a  $256 \times 256$  HgCdTe Rockwell array. NIC1, NIC2 and NIC3 have pixel sizes (and FOVs) of  $0.043''$  ( $11'' \times 11''$ ),  $0.075''$  ( $19.2'' \times 19.2''$ ) and  $0.2''$  ( $51.2'' \times 51.2''$ ), respectively. Due to deformation of the instrument’s dewar during heating, NIC3 was displaced sufficiently that it could not be brought into common focus with NIC1 and NIC2 during the time of our observations, so we obtained no useful data with this camera. Further details regarding the NICMOS instrument and its on-orbit performance can be found in Thompson et al. (1998).

All of our NICMOS observations were acquired in parallel using the MULTIACCUM observing mode and SAMP-SEQ settings of either STEP16, MIF512 or MIF1024 (exposure times of 304s, 514s or 1026s, respectively, in Table 2). We obtained NICMOS H-band images for the UMi and UMi-off fields described below (F160W for NIC2, F140W for NIC1; the latter very broad filter encompasses both J and H; we will refer to magnitudes in these filters as  $H_{160}$  and  $H_{140}$ , respectively). We also obtained NIC2 H-band data for the same M15 field for which we obtained STIS LP data (and for which there exist archival WFPC2 data, as discussed above and in Houdashelt et al. 2001), again facilitating a direct comparison of the UMi data with that of a known metal-poor, old population. These M15 data allowed the derivation of an  $I_{LP}$ ,  $H_{160}$  CMD that was used to place limits on the presence of faint red stars in the Ursa Minor dSph, as described below.

### 5.1. M15 NIC2 data

The M15 NIC2 datasets are summarised in Table 2 and were reduced using the standard IRAF tasks NICPIPE, `biaseq` and PEDSKY. These data were first reduced using the most up-to-date calibration files available from the HST pipeline; they were then reduced in a slightly different manner, substituting the synthetic, temperature-specific flats and temperature-dependent darks, which can be generated from the STScI web pages, for their pipeline analogs. Using the synthetic flats and darks produced a more uniform background in the STEP16 image, so both were used in the final reduction of these data. For the MIF512 data, the STScI database of dark images is evidently too sparse to allow a good interpolation to the temperature of interest (B. Monroe, private communication), as the pipeline darks proved far superior in removing the shading seen in NICMOS images. Thus, the pipeline darks and synthetic flats were used in this case. The calibrated STEP16 and MIF512 images were then combined through simple averaging, as there were no shifts between the images. Fig. 15 shows the resulting F160W image of M15.

Photometry was performed using the DAOPHOT software within IRAF. The positions of stars in the images were found using the task DAOFIND and adopting a  $3.5\sigma$  detection threshold. Aperture magnitudes were then calculated with the PHOT task using a 2 pixel aperture; for each star, the sky brightness was estimated from the mode in a circular annulus, centred on the star, having an inner radius of 6.67 pixels ( $\sim 0.5''$ ) and a width of 6.67 pixels. To derive the  $H_{160}$  magnitudes in an aperture having a radius of  $0.5''$ , aperture corrections were calculated from 8 bright, isolated stars in the image. The resultant aperture correction was  $-0.638 \pm 0.084$  ( $1\sigma$ ) mag. No psf photometry

was performed for the NICMOS data.

STIS-to-NICMOS coordinate transformations were calculated with the IRAF task `IMAGE`, using the positions of the stars used to compute the aperture corrections. This transformation was used to match the NICMOS and STIS detections, requiring that the predicted and measured positions agree within one NIC2 pixel. The resulting M15  $I_{LP}$ ,  $H_{160}$  colour-magnitude diagram is shown in Fig. 16.

## 5.2. UMi NICMOS data

The NIC1 and NIC2 datasets for the UMi dSph galaxy have coordinates  $(\alpha_{2000}, \delta_{2000}) = (15^h 08^m 41.41^s, +67^\circ 04' 08.51'')$  and  $(15^h 08^m 45.62^s, +67^\circ 03' 45.02'')$ , respectively, and are again summarised in Table 2. The NIC1 data do not contribute anything new to the conclusions and are discussed for completeness only.

The NIC2 data were reduced in the same manner as were the M15 NIC2 data, but always using the synthetic flats and darks in the calibration. Each set of 33 individual exposures was combined into a final image using a median. The images taken with the NIC1 camera (pixel scale of 43 mas/pixel) had only sub-pixel shifts among the data taken in 1997, but these were offset by 1–2 pixels from the 1998 data, so we aligned the NIC1 images before combination. The final image from NIC1 is shown in Fig. 17. The images taken with the NIC2 camera (pixel scale of 75 mas/pixel) were not shifted with respect to one another before being combined; as can be seen in the final image (Fig. 18), only one star is bright enough to be used in determining the relative positioning of the NIC2 images, and it unfortunately falls on a bad column, causing problems for the centering algorithm. In any case, only subpixel shifts are expected based on the NIC1 data, and blinking of several NIC2 images revealed no detectable shifts.

The detection limit of the UMi NICMOS data was determined by placing artificial stars in the NIC2 image and attempting to recover them using `DAOFIND`. Model psfs for a late K dwarf (K7 V) were created using the `TinyTim` software, assuming the appropriate camera and filter combination (F140W with NIC1; F160W with NIC2). However, the detector characteristics, and thus the `TinyTim` psfs, are dependent upon the date of observation (cf. Suchkov & Kriss 1998). As shown in Table 2, the bulk of our data were obtained in November, 1997, so for the level of accuracy required for our purposes, we simply adopted November 7, 1997, as the relevant date for input to `TinyTim`.

Considering input artificial stars in the magnitude range  $20 < H_{160} < 25$  (measured within an aperture of radius  $0.5''$ ) of fixed underlying spectral type (K7 V) and adding 5 stars per half-magnitude bin, 80% of stars at  $H_{160} = 23.5$  were recovered, while the recovered fraction at  $H_{160} = 24$  or fainter was less than 20%. We checked this limit further by analysing the UMi offset fields in a similar fashion and found a very similar detection limit of  $H_{160} = 24.0$  for the UMi-off-NIC2 field. We also determined limiting magnitudes of  $H_{140} = 24.3$  for the UMi-NIC1 field and  $H_{140} = 23.8$  for UMi-off-NIC1.

To further test these findings, we calculated the  $3\sigma$  fluctuation in the background by fitting a Gaussian to the histogram of counts/pixel in each combined image (excluding the tail to high counts). We then scaled the model psfs so that their central pixel was above the  $3\sigma$  background noise limit, and the average value of the four pixels surrounding the peak pixel was equal to this  $3\sigma$  value. Photometry of these normalised psfs was carried out using the APPHOT package in IRAF to derive magnitudes in a  $0.5''$  aperture. This provided another estimate of the detection limit for NIC2 of  $H_{160} = 24.2$  and for NIC1 of  $H_{140} = 24.3$ .

Aperture photometry, using the IRAF version of DAOPHOT, provided four stellar objects in the NIC1 image; these have  $H_{140}$  magnitudes between 21.27 and 24.40 in a  $0.5''$  aperture. Twelve stellar objects were detected in this manner in the NIC2 image – the bright star with  $H_{160} = 19.7$ , and eleven other objects with magnitudes between 22.89 and 24.25 – all consistent with our estimates of the detection limits. Reassuringly, the relative number counts do approximately scale with the sizes of the NIC1 and NIC2 fields of view.

## 6. Stellar Populations in UMi, M92 and M15

The globular clusters M92 and M15 were chosen as comparison clusters because their metallicities and ages are essentially the same as that of the dominant population in the UMi dSph; high-resolution spectroscopic studies give  $[Fe/H] \sim -2.2$  for both M92 and M15 (Snedden et al. 1991; Carretta & Gratton 1997; Shetrone, Côté & Sargent 2001). Furthermore, these clusters are also in low-reddening lines of sight and have deep HST/WFPC2 observations in the same filters as our observations (Piotto et al. 1997; photometry kindly made available to us by G. Piotto). The latter allowed us to perform our comparisons totally within the HST/WFPC2 in-flight filter system, eliminating the need to rely on the less well-determined colour transformations to the standard, ground-based Johnson-Cousins system.

### 6.1. Morphology in the Colour-Magnitude Diagram

#### 6.1.1. UMi-WFPC2 Field

The WFPC2 CMDs of the UMi dSph galaxy resulting from the psf photometry are given in Fig. 19, where we show the data from the three WF chips separately (for clarity) and also show the CMD from the entire dataset. Our CMD of the UMi dSph extends some 3 magnitudes deeper than the data analysed by Mighell & Burke (1999), and it is interesting to revisit a direct comparison with M92. We derived a fiducial ridge line for M92 in these HST bandpasses from the data of Piotto et al. (1997) by calculating the mean colour (and the standard deviation of this mean) in half-magnitude bins, then rejecting stars lying more than two sigma from the mean colour of their bin, and repeating this process until all remaining stars were within two sigma of the resulting ridge line (the algorithm outlined by Mighell & Burke, 1999, provides a consistent result).

This ridge line, moved to the distance modulus of the Ursa Minor dSph (adopted as 19.1 mag,

4.5 mag more distant than our adopted distance modulus of 14.6 mag for M92), is shown in the left-hand panel of Fig. 20, overlaid on our WFPC2 CMD of the UMi dSph. The remarkably good agreement in the overall morphology of the  $V_{606}, V_{606}-I_{814}$  CMD supports the contention that the dominant stellar population in the Ursa Minor dSph is old and metal-poor, very similar to that of classical halo globular clusters like M92.

The fiducial ridge line for the main sequence of the Ursa Minor dSph, obtained by applying the iterative procedure described above, is compared to that of M92 in the right-hand panel of Fig. 20. There is remarkably good agreement, especially since we have ignored the reddening, which is small, and hence any possible reddening differences; the reddening towards M92 is  $E(B-V) \sim 0.02$  (Harris 1996), perhaps 0.01 mag less than towards the UMi dSph field. The distance modulus offset adopted are clearly satisfactory. A direct (differential) comparison of the luminosity functions of M92 and the UMi dSph is supported as being equivalent to a comparison of their mass functions.

There is a small population of stars significantly bluer than the dominant (old) main-sequence turnoff, as previously noted (Olszewski & Aaronson 1985; Feltzing, Gilmore & Wyse 1999; Mighell & Burke 1999). Fig. 21 shows the CMD derived from all of the WFPC2 data for the UMi dSph, together with the M92 fiducial main sequence and metal-poor, old isochrones (VandenBerg & Bell 1985, transformed to HST bandpasses by G. Worthey). The distribution of these blue stars, those with  $V_{606} - I_{814} \lesssim 0.4$ , does not match the expected distribution predicted by younger isochrones of the same (low) metallicity as the bulk of the population. These stars are also too blue to be typical Galactic halo turnoff stars, which have a higher metallicity but a similar age to stars in the UMi dSph. The CMD of the UMi-off-WFPC2 field, discussed below, contains no such stars, strengthening their association with the Ursa Minor dSph. These few stars are in any case at brighter magnitudes than is relevant for our luminosity function comparison. They may well be ‘blue stragglers’, plausibly produced by mass transfer in close binaries (e.g. Leonard 1996), a conclusion also reached by Carrera et al. (2002) from their wide-area, ground-based investigation of the Ursa Minor dSph. While one might be surprised that close binaries form in such low-surface-density environments, the extreme red giants in the UMi dSph are CH-type carbon stars, also likely formed by mass transfer in binaries (Shetrone, Côté & Stetson 2001); we discuss the possible binarity of the stars on the UMi main sequence below.

### 6.1.2. *UMi-off-WFPC2 Field*

The CMD of the 21 unresolved objects in the control UMi-off-WFPC2 field, spanning a wide colour range and consisting of a mix of unresolved galaxies and Galactic foreground stars, is shown in Fig. 22. The colour and magnitude distribution of these objects is similar to that seen, for example, in the HDF (see Figure 3 of Elson, Santiago & Gilmore 1996). Comparison with the CMD of the Ursa Minor dSph shows that several of the UMi-off-WFPC2 objects lie in the vicinity of the main sequence of the dwarf galaxy, but represent only a minor contaminant. Background contamination is less than 1% of the UMi star counts at any given magnitude, leading to negligible uncertainty in the conclusions drawn from our luminosity functions.

## 7. Results and Luminosity Functions

### 7.1. The WFPC2-based Luminosity Functions

The WFPC2 luminosity functions for the UMi dSph are obtained by selecting only stars detected in both the F814W and V606W images, and further requiring the stars to lie within some range of the fiducial main sequence of the Ursa Minor dSph. The selection criteria appropriate to our errors are illustrated in Fig. 23. The star counts that met these criteria were then binned and corrected for incompleteness on a chip by chip basis, and the final luminosity function derived from their sum. The outcome is robust, as shown by experimenting with different choices of bin centres and with applying the completeness correction at various sub-bins across an individual luminosity function bin, all of which had negligible effect on the luminosity function in 0.5 magnitude bins. The final, completeness-corrected luminosity functions based on these selected main-sequence data are given in Table 9, where entries below the 50% completeness limit are denoted in parentheses. Note that the bright limit of the luminosity function derived in this manner from the CMD is shown on Fig. 23, and it is simply appended to the brighter, unselected data given in the earlier Tables 5 and 6.

Very few stellar objects were detected in both passbands in the UMi-off-WFPC2 field (see Fig. 22), and so these provide only a very minor contaminant to the derived luminosity functions of the Ursa Minor dSph, especially when required to lie near the UMi main sequence in colour and magnitude as here. We use the off-field data to determine the range of systematic uncertainty in our derived UMi luminosity functions due to unresolved faint sources being erroneously counted as member stars. Since the total exposure of the UMi-off field is not the same as that of the UMi field (due to the additional exposures acquired after failures of STIS) a simple count subtraction would not be appropriate. Rather we simply use the off-field data to demonstrate the very low amplitude of any likely effect of non-member stars on our derived luminosity functions of the UMi dSph.

Our results are shown in Fig. 24 and Fig. 25, where the  $I_{814}$  and  $V_{606}$  luminosity functions of the Ursa Minor dSph are compared to those of the globular clusters M92 and M15 (moved to the same distance modulus as that of the Ursa Minor dwarf spheroidal, a zero-point shift of 3.8 mag in apparent distance modulus for the M15 data, and normalised to the luminosity functions of the UMi dSph at  $V_{606} = 24.25$  and  $I_{814} = 23.25$ ). The absolute magnitude scale is given along the upper x-axis. It is clear from these figures that, down to the 50% completeness limits of the Ursa Minor data, there are negligible differences between the luminosity functions of these three stellar systems.

The slopes derived from linear, least-squares fits to the luminosity functions over the magnitude range 24 to 26.5 in  $I_{814}$  are  $0.184 \pm 0.025$  for the Ursa Minor dSph data,  $0.156 \pm 0.027$  for the M92 data, and  $0.218 \pm 0.012$  for the M15 luminosity function. The  $V_{606}$  slopes in the magnitude range 24.5 to 27.5 are, respectively,  $0.139 \pm 0.028$ ,  $0.154 \pm 0.026$  and  $0.187 \pm 0.017$  for the UMi dSph, M92 and M15. Any differences between the UMi dSph data and those of the globulars are less than  $2\sigma$ . We investigated the use of different magnitude ranges to determine the luminosity function slope and found generally consistent results.

As a means to quantify further the statistical significance of any differences, we performed Kolmogorov-Smirnov (K–S) tests (e.g. Press et al. 1992) on the unbinned (and not completeness-corrected) data. This test is most sensitive to differences between the middle ranges of the datasets, but we did take care to exclude the faintest bins (which are affected by incompleteness), and also the brightest bins (where small number statistics could cause problems). Unfortunately, the K–S test cannot account for systematics, and we found that the results were very sensitive to the exact distance modulus offset between the globular clusters and the UMi dSph; this lack of robustness degrades the usefulness of the K–S test. Nevertheless, comparing the data for M92 and for the UMi dSph, adopting our nominal distance modulus difference of 4.5 mag gives a probability of observing larger deviations, under the null hypothesis of the same underlying distribution, of only 1.4% for the I-band data and 4.4% for the V-band data. Recent investigations have indicated that the distance modulus of Ursa Minor may be a few tenths of a magnitude larger than our nominal value (e.g. Carrera et al. 2002), but it is not clear what this implies for the relative distance moduli. Increasing the distance modulus offset to 4.6 mag, within the uncertainties in distances and reddenings (the latter has been ignored thus far), increases these probabilities to 8% and 13% respectively. However, decreasing the distance modulus offset to 4.4 mag decreases the probabilities to less than 0.01%. Adopting the standard (conservative) significance level of 1% for a statistically significant detection of a difference in underlying distributions, there is only weak evidence for variations, and the simplest interpretation is that the underlying distributions are indeed the same.

One can also apply statistical tests to the binned data, with the usual approach adopted in comparisons being based on the  $\chi$ -square statistic (Press et al. 1992). Applying this test, under the same null hypothesis and considering similar magnitude regimes to those adopted for the K-S test above, gives probabilities of obtaining the given value of  $\chi$ -square or larger of 10% for the V-band, and 3% for the I-band, both allowing us to accept the null hypothesis that the UMi dSph and M92 luminosity functions are drawn from the same underlying distributions. Choosing different magnitude ranges and bin centers provide variations in these probabilities of factors of several, usually upwards; as with the K–S test, the conservative interpretation is that the underlying distributions are indeed consistent with each other.

## 7.2. The M15 STIS $I_{LP}$ Luminosity Function

The luminosity function derived from our STIS LP data for M15 is shown in the top panel of Fig. 26 and is tabulated in Table 7. This luminosity function is based on aperture photometry (the luminosity function constructed from psf-based magnitudes is not significantly different from that shown) and includes all of the stars detected and meeting the psf selection criteria described above.

The relation between  $I_{LP}$  and  $I_{814}$  derived from the fiducial M15 main sequence stars (see Houdashelt et al. 2001), given above in equation (1), can be used to transform our derived  $I_{LP}$  luminosity function into an  $I_{814}$  luminosity function, providing us with a consistency check. This STIS-derived  $I_{814}$  luminosity function of M15 is compared to the tabulated  $I_{814}$  luminosity function of Piotto et al. (1997) in the bottom panel of Fig. 26. The reddening and apparent V-band distance modulus used are  $E(B-V) = 0.1$  and 15.37 mag, respectively (Harris 1996); adopting  $A_V/E(B-$

$V) = 3.1$  gives a true distance modulus for M15 of  $(m-M)_0 = 15.06$ . The extinction in the HST filters was calculated as in Houdashelt et al. (2001), giving  $A_{814} = 0.60 A_V$  and  $A_{LP} = 0.68 A_V$ , to sufficient accuracy over the relevant range of stellar spectral types.

Using the models of Baraffe et al. (1997) and the transformations of Holtzman et al. (1995), the peak ( $M_{814} \sim 8.5$ ) and the 50% completeness limit ( $M_{814} \sim 10$ ) of our M15 luminosity function correspond to about  $0.27 M_\odot$  and  $0.15 M_\odot$ , respectively.

### 7.3. The UMi $I_{LP}$ Luminosity Function

Our final  $I_{LP}$  luminosity function of the UMi dSph, tabulated in Table 8, is derived from all of the objects detected in the UMi-STIS image that meet the psf selection criteria shown by the dashed lines in Fig. 8, after subtracting the objects in the UMi-off-STIS image that meet these same criteria. We corrected for the small reddening, to match the treatment of M15. We compare this luminosity function to the  $I_{LP}$  luminosity function of M15 in the lower panel of Fig. 27; due to the aforementioned uncertainties in the actual number of field stars and galaxies lying in the UMi-STIS field, the corresponding upper panel of this figure compares the M15 luminosity function to the UMi luminosity function that results when no correction is made for the ‘objects’ detected in the UMi-off-STIS field. The luminosity functions are adjusted slightly in normalisation for the best fit, and there is clearly no significant difference between the comparisons in the upper and lower panels. Fitting slopes to the final (subtracted) luminosity functions (0.5 mag bins) over the magnitude range with good statistics, namely the faintest six bins for UMi ( $25.75 \leq I_{LP} \leq 28.75$ ) and the six bins with  $22.25 \leq I_{LP} \leq 25.25$  for M15, gives a slope of  $0.244 \pm 0.023$  for the UMi dSph and a slope of  $0.261 \pm 0.013$  for M15. We tested the robustness of these slopes by shifting the bin centres of the luminosity functions by 0.25 mag and also by rebinning the luminosity functions in 0.25 mag bins. The former resulted in slopes of  $0.256 \pm 0.013$  for UMi and  $0.255 \pm 0.013$  for M15, while the latter gave slopes of  $0.250 \pm 0.020$  for UMi and  $0.252 \pm 0.013$  for M15. All of these estimates of the slopes of the STIS LP luminosity functions of M15 and the UMi dSph agree within  $\lesssim 1\sigma$ . K–S and  $\chi$ –square tests were applied as above; the K–S test on the off-field-subtracted data that are more than 80% complete, with no bright cut, gave a probability statistic of 22%, increasing to 57% if stars brighter than  $M_{LP,0} = 6.5$  were excluded. The  $\chi$ –square tests on the binned data give clear consistency among all the datasets, both off-subtracted, and not off-subtracted, for the UMi dSph, and M15 (probability statistics of greater than 30%), with the non-off-subtracted data providing the higher probability value (52%).

The statistical tests thus reinforce our conclusion that these two objects have indistinguishable faint luminosity functions, and hence initial mass functions, over the range of the data.

### 7.4. Comparison of $I_{814}$ UMi Luminosity Functions

Transforming the  $I_{LP}$  luminosity function to an  $I_{814}$  luminosity function by means of equation (1) provides an independent measure of the latter, and comparison with the directly measured

WFPC2  $I_{814}$  luminosity function allows a further test of the robustness of our results. This comparison is shown in Fig. 28, where the luminosity functions have been normalized in the magnitude range  $25 \leq I_{814} \leq 27$ . Fitting over the magnitude range  $22.75 \leq I_{814} \leq 26.75$ , the transformed luminosity function has slope  $0.219 \pm 0.031$ , within  $1\sigma$  of the slope of  $0.244 \pm 0.011$  for the WFPC2 luminosity function. The K–S test applied to the data over the range where they are more than 80% complete gives clear consistency again, with a probability statistic of 80%. The  $\chi$ –square test provides a probability of 58% that the derived value of  $\chi$ –square or larger could be obtained if the underlying distributions are the same. Thus, our characterisation of the  $I_{LP}$  luminosity function of the UMi dSph is consistent with the WFPC2 results. The transformation provides an equivalent  $I_{814}$  50% completeness limit of  $I_{814} = 27.4$ , a few tenths fainter than the direct WFPC2 data.

### 7.5. Things that go lump in the NICMOS data

The NIC2/NIC1 sensitivity limits are not as deep, for normal stars, as those of the STIS/LP or WFPC2 data, but do allow us to exclude any hypothetical population of very red stars. The NIC2  $H_{160}$  limiting magnitude may be transformed into a corresponding  $I_{LP}$  limit for main sequence stars in the UMi dSph using the M15  $H_{160}$ ,  $I_{LP} - H_{160}$  colour-magnitude diagram presented in Fig. 16, after taking account of the difference in distance moduli between M15 and UMi. For a main sequence star in the UMi dSph, a magnitude of  $H_{160} = 24$  (slightly fainter than the 50% completeness limit of the UMi-NIC2 data) corresponds to  $I_{LP} = 26.6$ , some  $\sim 2.5$  magnitudes brighter than the STIS LP 50% completeness limit for the UMi dataset,  $I_{LP} \sim 29$  mag.

A comparable CMD for the NIC1 filter, F140W, was derived by means of SYNPHOT transformations from NIC2/F160W, using input blackbody spectra having a range of temperatures. Applying the process outlined above to this transformed CMD leads to our NIC1 50% completeness limit corresponding to  $I_{LP} \sim 26.2$ , somewhat brighter than that derived from the NIC2 data.

The NICMOS data thus offer no new constraints on the number of stars with normal main sequence colours in UMi. However, a hypothetical population of faint red stars with  $I_{LP} \gtrsim 28.5$  and  $I_{LP} - H_{160} > 4.5$  (some 1.5 magnitudes redder than the nominal main sequence at that magnitude), would have been detected and thus is ruled out by the NICMOS data as being a substantial component of the Ursa Minor dSph.

## 8. Possible Complications

### 8.1. Binary Stars in the Ursa Minor dSph, M92 and M15

The evolution of close binary systems may create the very blue stars near the turnoff of the colour-magnitude diagram of the Ursa Minor dSph (blue stragglers), and also the very red giants in UMi (carbon stars that have magnitudes brighter than relevant for the present luminosity function analysis). In addition, unresolved binaries might affect the faint luminosity function comparisons, if the binary fraction, or the binary primary-secondary mass function, of the UMi dSph were very

different from that of M92 or of M15. Unresolved binary systems can be detected from analysis of the colour-magnitude data, since they provide a red asymmetry of several hundredths of a magnitude in the colour distribution of stars about the observed main sequence. Depending on the mass ratios within the binary systems, there will be a gradual spread of stars between the main sequence and the equal-mass binary sequence that lies about 0.75 mag brighter than the single-star main sequence (Hurley & Tout 1998). Even though  $V-I$  is not the most sensitive discriminator between single and binary stars, since the main sequence in the CMD becomes quite vertical in this colour, a spread to the red can clearly be seen in our WFPC2 colour-magnitude diagrams of the UMi dSph (see Figs. 19 and 20). We now proceed to quantify this visual impression of a redward asymmetry.

The investigation of the possible binary content required that we isolate a portion of the main sequence that is bright enough to have small enough photometric errors to be able to detect a redward spread, but still contains enough stars for statistical significance. Fig. 29 shows, for each WF chip and for M92 (moved to the distance of the Ursa Minor dSph), the portion of the upper main sequence that was selected, together with the fiducial ridge-line previously calculated from all of the Ursa Minor data. For each star in this region of the CMD, and for each chip separately, we then calculated the perpendicular distance to the ridge line. We determined the median distance from the ridge line for stars in each chip; minor differences were found, such that  $median(WF4) - median(WF2) = 0.010$  and  $median(WF4) - median(WF3) = -0.026$ , with the median for chip WF4 being  $-0.016$ . A small negative value for the overall median is expected, as the fiducial ridge line was constructed using the mean colour for all stars, both binary and single, and is thus slightly redder than the actual single-star main sequence.

For the purpose of studying the binary fraction, we adjusted the ridge-line offsets measured for stars in WF2 and WF3 so that their median values agreed with that for stars in WF4. This zero-point shift is equivalent to moving the ridge line in the direction perpendicular to it. A histogram of the resulting ridge-line offsets was then constructed and is shown in Fig. 30. The histogram is asymmetric, with a fairly steep rise on the blue side, reaching a flat-ish peak then falling off with a red excess, as expected for unresolved binaries of a range of mass ratios. As demonstrated by Hurley & Tout (1998), there is no simple way to invert the asymmetrical colour distribution into a fraction of stars in binaries of a given mass ratio distribution, but the amplitude of the asymmetry does provide a statistical detection of unresolved binaries.

We quantified the asymmetry by simply reflecting the histogram about its peak, and subtracting the ‘blue side’ from the ‘red side’; the remaining ‘stars’ in the excess on the red side are then candidates for being unresolved binaries. This procedure is illustrated in Fig. 30, and the shaded region for the histogram of the Ursa Minor dSph contains  $\sim 5\%$  of the total number of stars.

The small histogram in Fig. 30 shows the result of applying the same analysis to the HST/WFPC2 data (Piotto et al. 1997) for M92 (again measuring perpendicular distances from the Ursa Minor ridge line), and a red tail is again detected, with a similar asymmetry value. The amplitude of a red asymmetry in the main sequence of M15 may be quantified similarly using the WFPC2 photometry from Piotto et al. (1997). We earlier (Houdashelt et al. 2001) calculated the fiducial main-sequence ridge line of M15 using an iterative,  $3\sigma$ -rejection, *median*-colour ridge-finding algo-

rithm. A straightforward subtraction of the counts of the blue stars rejected during the derivation of the fiducial from the rejected red stars, yields a red excess amounting to  $\sim 6\%$  (in the magnitude range  $22 \leq V_{606} \leq 24.5$ ). This is consistent with the asymmetries derived for the main sequences of the Ursa Minor dSph and of M92.

It is not straightforward to characterize the binary population from the asymmetry in colour, but the similarity in the amplitudes that we find for the fields in the two globular clusters and in the Ursa Minor dSph does suggest that the binary populations are unlikely to be very disparate in these three systems (at least at the intermediate radius studied in the globular clusters). This further supports the reliability of using direct comparisons of their stellar luminosity functions to search for differences between their IMFs. In any case, for the relevant mass range the slope of the apparent luminosity function is not sensitive to variations in binarism of even  $\gtrsim 50\%$  (Kroupa, Gilmore & Tout 1991; their Figure 3 shows significant divergences only for stars less luminous than  $M_V > 11$ , even for the comparison of a single-star luminosity function against one with all stars in unresolved binaries), especially for magnitude bins as large as the 0.5 mag bins that we have adopted.

## 8.2. Are the globular cluster luminosity functions primordial?

Internal (two-body relaxation and mass segregation) and external (e.g. disk shocking) dynamical effects can influence the observed luminosity function at a given radius inside a globular cluster. Thus, prior to proceeding with the comparison between the Ursa Minor dSph and the globular clusters, it is important to establish that the luminosity functions that we and Piotto et al. (1997) have measured for the clusters are representative of those of the initial stellar populations; the cluster may have undergone dynamical evolution that could have caused stars of different masses to have different spatial distributions within the cluster. Mass segregation acts to increase the numbers of massive stars in the central regions, while populating the outer regions with low-mass stars, and thus would have the effect that the observed luminosity functions would be steeper at the faint end in the outer parts of the cluster than in the inner regions.

The Piotto, Cool & King (1997) data that we use, and our new STIS/LP data for M15, were obtained at intermediate radius within both M15 and M92, (at  $\sim 70$  and  $\sim 20$  core radii, respectively; note that M15 is very highly concentrated) where the effects of mass segregation are expected to be small and the local faint luminosity function should be a good estimate of the global (and initial) faint luminosity function, especially over the mass range relevant for our comparisons with the Ursa Minor dSph.

A test of this expectation for M92 is provided by the analysis of Andreuzzi et al. (2000), who derived luminosity functions from WFPC2  $V_{555}$  and  $I_{814}$  observations at  $\sim 13$  and  $\sim 21$  core radii, where one core radius is  $15''$  (Harris 1996). The data analysed by Andreuzzi et al. (from GO5969) are derived from pointings along an axis south of the cluster centre, while the field observed by Piotto et al. (1997) lies roughly north-east of the centre at around 22 core radii. The luminosity functions derived from each study are shown in Fig. 31, where the data have been shifted to the

distance modulus of the Ursa Minor dSph and normalized between  $25 < I_{814} < 26$ . The 50% completeness limit for the Ursa Minor data is also indicated in the figure. It is clear from this plot that, while there is evidence for mass segregation – the outer field has relatively more low-mass stars than the inner field – the luminosity functions of the three fields observed in M92 differ very little (at most 0.15 in the log, equal to the difference between the M92 and M15 luminosity functions at our 50% completeness limit) over the magnitude range in which we will compare the luminosity function of M92 with our Ursa Minor dSph data. Any significant difference caused by mass segregation in M92 is restricted to magnitudes that are fainter than our 50% completeness limit in the Ursa Minor dataset. There are no corresponding data for intermediate radii in M15.

As discussed by Elson et al. (1999) and by Piotto & Zoccali (1999), M92 and M15 have fairly steep main-sequence luminosity functions at intermediate radii, while other globular clusters, particularly those for which external dynamical effects such as tidal shocking by the disk or bulge of the Milky Way may be important, have flatter faint luminosity functions (and again these differences occur fainter than the 50% completeness limits of our present Ursa Minor dSph data). Indeed, analyses of the available estimates of the true space motions of globular clusters suggest that both M92 and M15 are fairly robust against both tidal shocking and evaporation (e.g. Dinescu, Girard & van Altena 1999).

Thus, the present-day faint luminosity functions of M92 and M15, at the locations observed and as faint as the magnitudes of interest, may be taken as reasonable estimates of the initial luminosity function in a low-metallicity, old system. A comparison between the luminosity functions of the Ursa Minor dSph and those of the clusters thus provides us with a direct comparison of the mass functions of these systems at formation.

### 8.3. Metallicity

We briefly discussed above the similarity of the  $V_{606}$ ,  $V_{606}-I_{814}$  colour-magnitude diagrams of the Ursa Minor dSph and M92. However, the  $V_{606}-I_{814}$  colour is rather insensitive to metallicity, as may be seen in Fig. 21, so that despite the narrowness of the RGB (cf. Mighell & Burke 1999), there could exist a range of metallicities within member stars of the Ursa Minor dwarf. The Wide Field Camera B–R data of Martínez-Delgado & Aparicio (1999) also show a narrow RGB; comparing the spread in their published CMD with the B–R,  $[\text{Fe}/\text{H}]$  relation for globular clusters (Harris 1996) suggests a dispersion of  $\sim 0.15$  dex. High-resolution spectra of six stars selected to cover the full colour width of the red giant branch of the Ursa Minor dSph (Shetrone, Côté & Sargent 2001) have a weighted mean iron abundance of  $[\text{Fe}/\text{H}] = -1.90 \pm 0.11$  and reveal a formal variation in metallicity of 0.3 dex, with most of the spread – and the bias to higher metallicity than that inferred for the bulk of the population – produced by one red, metal-rich star with a derived  $[\text{Fe}/\text{H}] \sim -1.45$ . This range in metallicity could result from self-enrichment, leading to the expectation that the more metal-rich stars are younger. A range of ages in the dominant ‘old’ population is indeed formally consistent with the star formation history derived by Hernandez, Gilmore & Valls-Gabaud (2000), given the reduced sensitivity of isochrones to ages older than  $\sim 10$  Gyr.

For old stellar systems, elemental ratios potentially allow finer relative age resolution than is possible using isochrones. An extended star-formation history with self-enrichment over longer than  $\sim 1$  Gyr – of order ten internal crossing times in the dSph – would perhaps be imprinted in the elemental abundances, since iron from the relatively long-lived Type Ia supernovae could be incorporated in the interstellar material from which the younger stars formed. This would result in lower values of the ratio of the alpha elements to iron in the younger stars, than in those stars that formed early from gas enriched by only massive stars through Type II supernovae (cf. Wheeler, Sneden & Truran 1989; Gilmore, Wyse & Kuijken 1989; Gilmore & Wyse 1991, 1998). Thus, an extended star formation history would provide an intermediate-age population with lower (i.e. close to the solar value) ratios of the alpha-elements to iron, and this is expected (cf. Unavane, Wyse & Gilmore 1996) and observed (Shetrone, Côté & Sargent 2001) for the bulk of the populations in the dwarf companion galaxies of the Milky Way. A star-formation history in which the bulk of the stars formed in the first  $\sim 1$  Gyr, with a subsequent low rate of star formation and self-enrichment, would produce a dominant stellar population with enhanced (compared to the solar value) ratios of the alpha elements to iron, plus a small, younger, more metal-rich population with lower values of this ratio.

The pattern of element ratios seen in the Ursa Minor stars fits this expectation, with the elemental abundance ratios in the metal-poor members of the Ursa Minor dSph equal to those of M92 stars (Shetrone, Côté & Sargent 2001), but with the more metal-rich stars having lower values of the ratio of alpha elements to iron. The comparison between the elemental abundances for member stars of the Ursa Minor dSph, of M92 and of the globular cluster M3 ( $[\text{Fe}/\text{H}] \sim -1.5$ ) is shown in Figure 32, with data taken from Shetrone, Côté & Sargent. Such an internal comparison, with all elemental ratios derived in the same investigation, is the most robust approach. The stars in the UMi dSph were chosen to cover the entire range of metallicity, and thus the spread of the member stars here is not representative of the intrinsic metallicity distribution of the UMi dSph, which is indicated by the smooth Gaussian in the bottom panel. Most of the stars in the UMi dSph, represented by the metal-poor member stars here, have elemental abundance ratios the same as the member stars in the globular clusters, i.e. enhanced alpha elements, indicative of Type II supernova enrichment. The more metal-rich stars in this system are consistent with forming from more iron-enriched gas, indicative of forming after the onset of Type I supernovae. This pattern is as expected from the star formation history inferred from the colour-magnitude diagram. Thus, the available chemical abundance data for the Ursa Minor dSph are consistent with a dominant population of old, metal-poor stars that formed in a short period ( $\lesssim 10^9$ yr), with an additional small population of more enriched, younger stars.

#### 8.4. Lumps in the Ursa Minor dSph?

The Ursa Minor dSph has very elliptical stellar isopleths, with an axial ratio of  $\sim 2:1$  (Irwin & Hatzidimitriou 1995; Kleyana et al. 1998). The available proper-motion data (Schweitzer, Cudworth & Majewski 1997) are consistent with the elongation being along the orbit, as expected if tides play an important role. Wide-area star counts have shown evidence for ‘extra-tidal’ stars (Irwin

& Hatzidimitriou 1995; Martínez-Delgado et al. 2001; Palma et al. 2002), though their existence and level of significance depend on uncertain background subtraction and the relevance of the King models used to determine the tidal radius, respectively. Rotation about the major axis (‘minor-axis rotation’) could be a signature of tidal effects and has been detected in the internal kinematics of the UMi dSph, but with low statistical significance, by Hargreaves et al. (1994) in their radial-velocity data extending  $\sim 150$  pc along the minor axis (and  $\sim 400$  pc along the major axis). Further intriguing suggestions of structure in the star counts (‘clumps’), with no variation in other properties of the stellar population (e.g. colour), have been reported since their initial tentative identification by Olszewski & Aaronson (1985). This is extremely unexpected for a system with a stellar velocity dispersion of  $\sim 10$  km/s ( $\sim 10$  kpc/Gyr), a characteristic radius of  $\lesssim 1$  kpc, and stellar ages of  $\gtrsim 10$  Gyr, much longer than the crossing time of  $\lesssim 10^8$  yr. The deeper data of Kleyana et al. (1998) show that the secondary peak in the stellar surface density seen in earlier work is significant only at the  $\lesssim 2\sigma$  level, but they do find another asymmetry at the  $3\sigma$  level. Eskridge & Schweizer (2001), in their proper-motion sample (limiting magnitude  $V \sim 20.5$ ), also find internal substructure on scales of a few arcmin, at a 99.5% confidence level.

The relative star counts in the various detectors discussed here similarly show low-level fluctuations, e.g. the counts in the NICMOS fields are a factor of  $\sim 2$  below the expectation from the STIS counts at the corresponding magnitude, and the STIS counts are perhaps 50% higher than expected from the WFPC2 counts in the same magnitude range. However, even if one were to conclude that the clumps and extra-tidal features were real, and hence that there were real phase-space structure in the UMi dSph, the interpretation of the line-of-sight velocity dispersion as reflecting a high mass-to-light ratio remains valid in all situations except complete disruption (cf. Piatek & Pryor 1995; Klessen & Kroupa 1998). The Ursa Minor dSph is most likely dark-matter dominated.

## 9. Implications

We show that the faint main-sequence stellar luminosity function of the Local Group dwarf spheroidal galaxy in Ursa Minor is indistinguishable from that of two classical halo globular clusters. The simplicity and similarity of the stellar populations in these systems allow us to make the further statement that the *mass* functions are essentially identical. Thus, in an old system with a high amount of inferred dark matter, the Ursa Minor dSph, and in an old system with no dark matter, a globular cluster, the stellar formation processes are such that the relative numbers of low-mass stars are the same. Furthermore, these two systems – a globular cluster and a dSph galaxy – are at opposite extremes of stellar surface density, with the central V-band surface brightness of M92 being 15.6 mag/sq arcsec (Harris 1996), while that of the UMi dSph is 25.5 mag/sq arcsec (Mateo 1998).

The stellar masses corresponding to our faintest (WFPC2) 50% completeness limits for the UMi dSph,  $V_{606} = 28.35$  and  $I_{814} = 27.19$ , may be estimated from stellar models. Using standard transformations from the appropriate HST filters to ground-based systems (Holtzman et al. 1995) and at the distance and reddening [ $E(V-I) \sim 0.045$ ,  $A_{606} = 0.88 A_V$ ] of the UMi dSph, the models of Baraffe et al. (1997) for low-mass stars of metallicity  $-2$  dex translate these completeness levels to

masses of  $\sim 0.3 M_{\odot}$  (V-band) and  $\sim 0.33 M_{\odot}$  (I-band). The Vandenberg isochrones (Vandenberg & Bell 1985) for  $[\text{Fe}/\text{H}] = -2.2$  dex, transformed into the HST filters by G. Worthey (priv. comm.), provide consistent results. The mass equivalent of the 50% completeness limit of the STIS-LP data, transformed into  $I_{814}$  using equation (1) above, is  $\lesssim 0.3 M_{\odot}$ . Thus, all of our luminosity functions consistently reach  $\sim 0.3 M_{\odot}$ .

We used the Baraffe et al. (1997) models to convert our  $I_{814}$  luminosity function for the UMi dSph (transformed from  $I_{\text{LP}}$ ) into a mass function, and we then performed a linear, least-squares fit to  $\log(\text{dN}/\text{dM})$  as a function of  $\log(M)$ . This gave a power-law slope for the resulting mass function of  $-1.8$  (where the Salpeter slope is  $-2.35$ ). The luminosity function that the Baraffe et al. models predict for a power-law mass function with this slope is shown in Fig. 33, and is clearly an acceptable fit to the observed luminosity functions.

### 9.1. Baryonic Dark Matter

The globular cluster luminosity functions to which we compare our data for the UMi dSph extend down to an equivalent mass of  $\lesssim 0.15 M_{\odot}$ , with no sign of an upturn in inferred mass function fit (Piotto & Zoccali 1999). The total mass-to-light ratios, based on observed internal kinematics, for these systems are low, only  $(M/L)_V \sim 2 - 3$  (Meylan 2001; see also Gebhardt et al. 1997). As discussed in Piotto & Zoccali (1999), at low masses,  $\lesssim 0.5 M_{\odot}$ , the inferred mass function for globular clusters is flatter than the Salpeter (1955) function; the actual form is rather uncertain, but as shown in their Figures 15 and 16, a mass function with a power law slope of close to  $-1.3$  (with Salpeter being  $-2.35$ ) is not unreasonable. The power-law slope that appears to provide a good fit to the UMi data is steeper than this (see Fig. 33, where a power law of slope  $-1.8$  is plotted), but is constrained only by stars down to our 50% completeness of  $\sim 0.3 M_{\odot}$ , where the effective power law may be expected to be closer to the steeper (Salpeter?) value of higher masses. Given the similarity in derived luminosity functions, the mass functions should indeed be consistent.

Assuming that a low-mass slope of  $-1.3$  provides a V-band mass-to-light ratio of 3, then, in the approximation that changing the slope of the low-mass mass function changes only the mass, adopting the Baraffe et al. models gives that a mass-to-light ratio of  $\sim 80$  (as quoted for the Ursa Minor dSph in Mateo 1998) would require a significantly steeper slope of  $-3.6$ . An alternative set of assumptions, that the low-mass slope of  $-1.8$  provides a  $M/L_V$  ratio of 2, gives that increasing the M/L ratio to 80 would require a slope of  $-4.15$ . The predictions for a slope of  $-3.66$  is shown in Fig. 34, and even this value is clearly not favoured by the observations, with the steeper slopes less compatible with the data. Of course, we cannot rule out a steep upturn fainter than our limit, and indeed a  $0.15 M_{\odot}$  star of metallicity  $-2$  dex has a V-band mass-to-light ratio of  $\sim 70$  (again using the Baraffe et al. models), so that a large population of stars around this mass could provide the mass. However, without this rather contrived IMF, our results imply that any baryonic dark matter in the UMi dSph is not associated with low-mass stars. This would be consistent with the null results from deep imaging of edge-on, late-type spiral galaxies with ISO at  $7\mu\text{m}$  and  $15\mu\text{m}$  (Gilmore & Unavane 1998) that exclude hydrogen-burning objects, down to the brown dwarf limit,

from making a significant contribution to the dark haloes inferred for those galaxies from rotation curves.

## 9.2. Universality of the IMF

The form of the stellar initial mass function is an important parameter, determining in large part the visibility of galaxies at high redshift, their contributions to the background light in various passbands, their chemical enrichment and gas consumption, and, through feedback processes, perhaps the star formation process itself. Low-mass stars have main-sequence lifetimes of order the age of the Universe, so simple counts of main-sequence stars provide the shape of the initial low-mass luminosity function, with essentially no corrections needed for finite stellar lifetimes.

We have demonstrated here that the faint luminosity function in the Ursa Minor dSph galaxy is indistinguishable from that in classical halo globular clusters. The only other derivation of a luminosity function for a dSph is that by Grillmair et al. (1998) for the upper main sequence of the Draco dSph galaxy, some three magnitudes brighter than the present data; in that galaxy, the analysis is complicated by the more significant metallicity spread (e.g. Shetrone, Bolte & Stetson 1998) and possible age spread (e.g. Aparicio, Carrera & Martínez-Delgado 2001) in the stellar population. However, the results are consistent with those presented here.

This flattening of the mass function slope is also consistent with the mass function inferred from HST/NICMOS data for the Galactic bulge, which was observed along a low-reddening line of sight at a projected distance from the Galactic centre of  $\sim 800$  pc and provides a luminosity function that is complete down to an equivalent mass of  $\sim 0.15M_{\odot}$ , close to the brown dwarf limit (Zoccali et al. 2000). As shown in that paper, the derived mass function is very similar to that of the globular cluster M15, and the Baraffe et al. models with power-law mass function slope flatter than the Salpeter (1955) value provide an acceptable fit (those authors compare their results with an IMF of slope  $-1.33$ , where Salpeter is  $-2.35$ ). The dominant stellar population in the bulge is old, perhaps as old as the globular clusters (Ortolani et al. 1995; Feltzing & Gilmore 2000), and metal-rich, with peak metallicity close to that in the solar neighbourhood, i.e. about half the solar value (e.g. McWilliam & Rich 1994; Rich & McWilliam 2000). Thus, the low-mass IMF of stars that formed at high redshift is apparently independent of metallicity.

While the age range of stars in the Ursa Minor dwarf spheroidal galaxy is small in a cosmological context, being at most a few Gyr and consistent with a much shorter duration, it is significantly larger than that believed to be the case for the globular clusters, where a duration of star formation of perhaps  $10^7$  yr is considered reasonable. Indeed, the inferred star formation rate during the epoch of most intense star formation in the UMi dSph is only some  $6 \times 10^{-4} M_{\odot}/\text{yr}$  (Hernandez, Gilmore & Valls-Gabaud 2000), many orders of magnitude below the few tenths of a solar mass per year inferred for a typical globular cluster. Thus, the low-mass IMF of stars that formed at high redshift is apparently independent of star formation *rate* also.

The faint luminosity function and low-mass IMF of stars formed recently are difficult to establish; in very young systems, one must often deal with the complexities of infrared luminosity

functions (cf. Muench, Lada & Lada 2000), and the interpretation of field star counts is complicated by the errors in luminosity introduced by distance uncertainties and unknown metallicity spreads. That said, the available data are consistent with a mass function again indistinguishable from that of the globular clusters (von Hippel et al. 1996; Reid et al. 1999; Gilmore 2001; Kroupa 2002; but see Eisenhauer 2001 for the view that the IMF does vary). Thus, the low-mass IMF is apparently invariant with time as well.

The *high-mass* IMF at early times cannot be observed today at low redshift, but it can be constrained by the chemical enrichment signatures left in the low-mass, long-lived stars that the massive stars enriched (cf. Wyse & Gilmore 1992; Wyse 1998). A massive-star IMF biased towards more massive stars will produce relatively higher ratios of the alpha elements to iron, due to the dependence of the alpha-element yields on Type II supernova progenitor mass (the actual value of this ratio is hard to predict based on current supernova nucleosynthesis models, but all calculations imply that there should be a dependence on the massive-star IMF; see Fig. 1 of Gibson 1998). Those stars in the Ursa Minor dSph observed with high-resolution spectroscopy (Shetrone, Côté & Sargent 2001), shown here in Fig. 32, have the classic halo ‘Type II plateau’ in the ratio of alpha-elements to iron at low metallicities. The more metal-rich stars in the Ursa Minor dSph have lower values of the ratio of  $[\alpha/\text{Fe}]$ , consistent with the incorporation of some iron from Type Ia supernovae, as would be expected if these more enriched stars formed after the more metal-rich stars, and  $\gtrsim 1\text{Gyr}$  after the onset of star formation in the galaxy. The absolute value of the ‘alpha-enhancement’ is similar for UMi stars with  $[\text{Fe}/\text{H}] \lesssim -2$ , for members of M92, and for field halo stars in the same metallicity range. This requires a similar (mass-averaged) IMF for stars more massive than  $\sim 9M_{\odot}$ , the progenitors of the Type II supernovae which largely created the alpha elements (cf. Wyse & Gilmore 1992). All indications (see e.g. the recent review by Kroupa 2002) are that this massive-star IMF is close to a power law having a slope consistent with the value derived by Salpeter (1955).

## 10. Summary and conclusions

Low-mass stars, those with main-sequence lifetimes that are of order the age of the Universe, provide unique constraints on the Initial Mass Function (IMF) when they formed. Star counts in systems with simple star-formation histories are particularly straightforward to interpret, and those in ‘old’ systems allow one to determine the low-mass stellar IMF at large look-back times and thus at high redshift. As described here, the main-sequence stellar luminosity function of the Ursa Minor dSph galaxy, and the implied IMF down to  $\sim 0.3 M_{\odot}$ , is indistinguishable from that of the halo globular clusters M92 and M15, systems with the same old age and low metallicity as the stars in the Ursa Minor dSph. The available (indirect) limits on the high-mass IMF, inferred from elemental abundance ratios, are also consistent with the same IMF in these two very different classes of systems. However, the globular clusters show no evidence for dark matter, while the Ursa Minor dSph is apparently very dark-matter dominated.

Thus, the low-mass stellar IMF for stars that formed at high redshift is invariant in going from a low-surface-brightness, dark-matter-dominated external galaxy to a globular cluster within

the Milky Way. The corresponding luminosity functions are in agreement with those derived for the field stars of the Milky Way bulge (Zoccali et al. 2000) and are consistent with those of the field halo and disk of the Milky Way (e.g. von Hippel et al. 1996; Kroupa, Tout & Gilmore 1993). Further, the elemental abundance ratios in these various environments are also consistent with being produced in supernovae of the same mix of progenitor masses. As a whole, the data support the concept of a universal IMF. This allows great simplification in models of galaxy formation and evolution, but begs the question, ‘Why?’

Support for this work was provided by NASA grant number GO-7419 from STScI, operated by AURA Inc., under NASA contract NAS5-26555. RFGW acknowledges the support of the PPARC Visitor Grant program, and thanks all those in the Astrophysics groups in St Andrews and Oxford for making her visits so enjoyable. SF acknowledges a travel grant from the Royal Swedish Academy which supported a visit to the IoA to facilitate this work.

## REFERENCES

- Andreuzzi, G., Buonanno, R., Fusi Pecci, F., Iannicola, G. & Marconi, G. 2000, *A&A*, 353, 944
- Aparicio, A., Carrera, R. & Martínez-Delgado, D. 2001, *AJ*, 122, 2524
- Bahcall, N. A., Ostriker, J. P., Perlmutter, S. & Steinhardt, P. J. 1999, *Sci*, 284, 1481
- Baraffe, I., Chabrier, G., Allard, F. & Hauschildt, P. H. 1997, *A&A*, 327, 1054
- Bellazzini, M., Fusi Pecci, F., Messineo, M., Monaco, L. & Rood, R. T. 2002, *AJ*, 123, 1509
- Carrera, R., Aparicio, A., Martínez-Delgado, D. & Alonso-García, J. 2002, *AJ*, in press (astro-ph/0203300)
- Carretta, E. & Gratton, R. G. 1997, *A&AS*, 121, 95
- Cool, A. M. & King, I. R. 1996, in ‘Calibrating Hubble Space Telescope: Post Servicing Mission’, eds. A Koratkar & C. Leitherer (Baltimore: STScI), p. 290
- D’Antona, F. 1998, in ‘The Stellar Initial Mass Function’, ASP Conf. Ser. Vol. 142, eds. G. Gilmore & D. Howell (San Francisco: ASP), p. 157
- De Marchi, G. & Paresce, F. 1995, *A&A*, 304, 202
- Dekel, A. & Silk, J. 1986, *ApJ*, 303, 39
- Dinescu, D. I., Girard, T. M. & van Altena, W. F. 1999, *AJ*, 117, 1792
- Eisenhauer, F. 2001, in ‘Starburst Galaxies: Near and Far’, eds. L. Tacconi & D. Lutz, (Berlin Heidelberg: Springer-Verlag), p. 24
- Elson, R. A. W., Santiago, B. & Gilmore, G. 1996, *New Astr*, 1, 1

- Elson, R. A. W, Tanvir, N., Gilmore, G., Johnson, R. A. & Beaulieu, S. 1999, in ‘New Views of the Magellanic Clouds’, IAU Symp. 190, eds. Y.-H. Chu, N. Suntzeff, J. Hesser & D. Bohlender (San Francisco: ASP), p. 417
- Eskridge, P. B. & Schweizer, A. E. 2001, *AJ*, 122, 3106
- Feltzing, S. & Gilmore, G. 2000, *A&A*, 355, 949
- Feltzing, S., Gilmore, G. & Wyse, R. F. G. 1999, *ApJ*, 516, L17
- Fruchter, A. & Hook, R. N. 1997, *SPIE*, 3164, 120
- Fruchter, A. S. & Mutchler, M. 1998, STScI preprint (available from [www-int.stsci.edu/~fruchter/dither/ditherII.ps](http://www-int.stsci.edu/~fruchter/dither/ditherII.ps))
- Gallagher, J. S. & Wyse, R. F. G. 1994, *PASP*, 106, 1225
- Gardner, J. P., et al. 2000, *AJ*, 119, 486
- Gebhardt, K., Pryor, C., Williams, T.B., Hesser, J. & Stetson, P. 1997, *AJ*, 113, 1026
- Gerhard, O. E. & Spergel, D. N. 1992, *ApJ*, 389, L9
- Gibson, B. 1998, *ApJ*, 501, 675
- Gilmore, G. 2001, in ‘Starburst Galaxies: Near and Far’, eds. L. Tacconi & D. Lutz (Berlin Heidelberg: Springer-Verlag), p. 34
- Gilmore, G. 1981, *MNRAS*, 195, 183
- Gilmore, G. & Howell, D. 1998, eds. ‘The Stellar Initial Mass Function’, ASP Conf. Ser. Vol. 142 (San Francisco: ASP)
- Gilmore, G. & Wyse, R. F. G. 1991, *ApJ*, 367, L55
- Gilmore, G. & Wyse, R. F. G. 1998, *AJ*, 116, 748
- Gilmore, G., Wyse, R. F. G. & Kuijken, K. 1989, *ARA&A*, 27, 555
- Gilmore, G. & Unavane, M. 1998, *MNRAS*, 301, 813
- Gonzaga, S., Biretta, J., Wiggs, M. S., Hsu, J. C., Smith, T. E., Bergeron, L., & the STScI WFPC2 Group 1998, WFPC2 ISR 98-04
- Grillmair, C. J., et al. 1998, *AJ*, 115, 144
- Hansen, B. M. S. 1999, *ApJ*, 520, 680
- Hargreaves, J., Gilmore, G. & Annan, C. 1996, *MNRAS*, 279, 108
- Hargreaves, J. C., Gilmore, G., Irwin, M. J. & Carter, D. 1994, *MNRAS*, 271, 693

- Harris, W. E. 1996, *AJ*, 112, 1487
- Hernandez, X., Gilmore, G. & Valls-Gabaud, D. 2000, *MNRAS*, 317, 831
- Holtzman, J. A., Burrows, C. J., Casertano, S., Hester, J. J., Trauger, J. T., Watson, A. M. & Worthey, G. 1995, *PASP*, 107, 1065
- Houdashelt, M. L., Wyse, R. F. G., & Gilmore, G. 2001, *PASP*, 113, 49
- Hurley, J. & Tout, C. A. 1998, *MNRAS*, 300, 977
- Irwin, M. & Hatzidimitriou, D. 1995, *MNRAS*, 277, 1354
- Johnson, J. A. & Bolte, M. 1998, *AJ*, 115, 693
- Kimble, R. A., et al. 1998, *ApJ*, 492, L83
- Klessen, R. S. & Kroupa, P., 1998, *ApJ*, 498, 143
- Kleyna, J. T., Wilkinson, M. I., Evans, N. W. & Gilmore, G. 2001, *ApJ*, 563, L115
- Kleyna, J. T., Geller, M. J., Kenyon, S. J., Kurtz, M. J. & Thorstensen, J. R. 1998, *AJ*, 115, 2359
- Kroupa, P. 2002, *Science*, 295, 82
- Kroupa, P., Gilmore, G. & Tout, C. A. 1991, *MNRAS*, 251, 293
- Kroupa, P., Tout, C. A. & Gilmore, G. 1993, *MNRAS*, 262, 545
- Leonard, P. J. T. 1996, *ApJ*, 470, 521
- Madau, P. & Pozzetti, L. 2000, *MNRAS*, 312, L9
- Martínez-Delgado, D. & Aparicio, A. 1999, in ‘The Stellar Content of Local Group Galaxies’, IAU Symp. 192, eds. P. Whitelock & R. Cannon (San Francisco: ASP) p. 179
- Martínez-Delgado, D., Alonso-García, J., Aparicio, A. & Gómez-Flechoso, M. A. 2001, *ApJ*, 549, L63
- Mateo, M. 1998, *ARA&A*, 36, 435
- McWilliam, A. & Rich, R. M. 1994, *ApJS*, 91, 749
- Meylan, G. 2001, in ‘Extragalactic Star Clusters’, IAU Symp. 207, eds. E. Grebel, D. Geisler & D. Minniti, in press (astro-ph/0107063)
- Mighell, K. J. & Burke, C. J. 1999, *AJ*, 118, 366
- Muench, A. A., Lada, E. A. & Lada, C. J. 2000, *ApJ*, 533, 358
- Olszewski, E. W. & Aaronson, M. 1985, *AJ*, 90, 2221

- Ortolani, S., Renzini, A., Gilmozzi, R., Marconi, G., Barbuy, B., Bica, E. & Rich, R. M. 1995, *Nature*, 377, 701
- Palma, C., Majewski, S., Siegel, M., Patterson, R. & Ostheimer, J. 2002, *AJ* submitted (astro-ph/0205194)
- Piatek, S. & Pryor, C. 1995, *AJ*, 109, 1071
- Piotto, G. & Zoccali, M. 1999, *A&A*, 345, 485
- Piotto, G., Cool, A. M. & King, I. R. 1997, *AJ*, 113, 1345
- Press, W. H., Flannery, B. P., Teukolsky, S. A. & Vetterling, W. T. 1992, ‘Numerical Recipes’, Cambridge University Press.
- Reid, I. N., Kirkpatrick, J. D., Liebert, J., Burrows, A., Gizis, J. E., Burgasser, A., Dahn, C. C., Monet, D., Cutri, R., Beichman, C. A. & Skrutskie, M. 1999, *ApJ*, 521, 613
- Rich, R. M. & McWilliam, A. 2000, *SPIE*, 4005, 150
- Salpeter, E. E. 1955, *ApJ*, 121, 161
- Schlegel, D. J., Finkbeiner, D. P. & Davis, M. 1998, *ApJ*, 500, 525
- Schweitzer, A. E., Cudworth, K. M. & Majewski, S. R. 1997, in ‘Proper Motions and Galactic Astronomy’, ASP Conf. Ser. Vol. 127, ed. R. M. Humphrey (San Francisco: ASP) p. 103
- Shetrone, M. D., Bolte, M. & Stetson, P. B. 1998, *AJ*, 115, 1888
- Shetrone, M. D., Côté, P. & Sargent, W. L. W. 2001, *ApJ*, 548, 592
- Shetrone, M. D., Côté, P. & Stetson, P. B. 2001, *PASP*, 113, 1122
- Snedden, C., Kraft R. P., Prosser, C. F. & Langer, G. E. 1991, *AJ*, 102, 2001
- Stetson, P. B. 1984, *PASP*, 96, 128
- Suchkov, A. & Kriss, J. 1998, NICMOS ISR-98-018
- Thompson, R. I., Rieke, M., Schneider, G., Hines, D. C. & Corbin, M. R. 1998, *ApJ*, 492, L95
- Tremaine, S. & Gunn, J. E. 1979, *Phys Rev Let*, 42, 407
- Unavane, M., Wyse, R. F. G. & Gilmore, G. 1996, *MNRAS*, 278, 727
- VandenBerg, D. A. & Bell, R. A. 1985, *ApJS*, 58, 561
- von Hippel, T., Gilmore, G., Tanvir, N., Robinson, D. & Jones, D. H. P. 1996, *AJ*, 112, 192
- Wheeler, J. C., Sneden, C. & Truran, J. W. 1989, *ARAA*, 27, 279
- Whitmore, B., Heyer, I., Casertano, S. 1999, *PASP*, 111, 1559

Woodgate, B. E., et al. 1998, *PASP*, 110, 1183

Wyse, R. F. G. 1998, in ‘The Stellar Initial Mass Function’, *ASP Conf. Ser. Vol. 142*, eds. G. Gilmore & D. Howell (San Francisco: ASP), p. 89

Wyse, R. F. G. & Gilmore, G. 1992, *AJ*, 104, 144

Zinn, R. 1981, *ApJ*, 251, 52

Zoccali, M., Cassisi, S., Frogel, J. A., Gould, A., Ortolani, S., Renzini, A., Rich, R. M. & Stephens, A. W. 2000, *ApJ*, 530, 418

Table 1. Properties of the Ursa Minor dSph.

Quantity	Value	Ref.
$(m - M)_o$	$19.1 \pm 0.1$	Mateo (1998)
Distance	65 kpc	
$E(B - V)$	$0.03 \pm 0.02$	Zinn (1981)
Central coordinates	$\alpha_{2000} = 15^h 08^m 59.6^s, \delta_{2000} = +67^\circ 13' 09''$	Kleyna et al. (1998)
Core radius	$\sim 15' \rightarrow \sim 275$ pc	Kleyna et al. (1998)
Tidal radius	$\sim 40' \rightarrow \sim 730$ pc	Kleyna et al. (1998)
$\Sigma_{V,central}$	25.5 mag/sq arcsec	Mateo (1998)
Integrated luminosity	$2 \times 10^5 L_{V,\odot}$	Kleyna et al. (1998)
$\langle [\text{Fe}/\text{H}] \rangle$	$\sim -2$ dex	Stetson (1984); Shetrone et al. (2001)
$\sigma_{[\text{Fe}/\text{H}]}$	$\lesssim 0.2$ dex	Stetson (1984)
$\sigma_{velocity,core}$	$7.5^{+1.0}_{-0.9}$ km/s	Hargreaves et al. (1994)
$(M/L)_{V,core}$	$59^{+41}_{-25} (M_\odot/L_{V,\odot})$	Hargreaves et al. (1994)
$(M/L)_{V,tot}$	79 $(M_\odot/L_{V,\odot})$	Mateo (1998)
SFR history	dominant early burst	Hernandez et al. (2000)

Table 2. The HST datasets GO 7419.

Field	Filter	Exposure (sec)	Date
UMi-WFPC2	F606W	1200 × 8	Nov 1997
	F606W	1200 × 2	Nov 1998
	F606W	1300 × 2	Nov 1999
	F814W	1200 × 8	Nov 1997
	F814W	1200 × 2	Nov 1998
	F814W	1300 × 4	Nov 1999
UMi-Off-WFPC2	F606W	1200 × 8	Nov 1997
	F814W	1200 × 8	Nov 1997
UMi-STIS	LP	2900 × 5	Nov 1997
	LP	2900 × 2	Nov 1998
	LP	3000 × 3	Nov 1999
UMi-Off-STIS	LP	2900 × 8	Nov 1997
UMi-NIC1	F140W	514 × 15	Nov 1997
	F140W	1026 × 9	Nov 1997
	F140W	514 × 6	Nov 1998
	F140W	1026 × 3	Nov 1998
UMi-NIC2	F160W	514 × 8	Nov 1997
	F160W	1026 × 16	Nov 1997
	F160W	514 × 3	Nov 1998
	F160W	1026 × 6	Nov 1998
M15	STIS-LP	1200	Aug 1998
M15 MIF512	NIC2-F160W	514	Aug 1998
M15 STEP16	NIC2-F160W	304	Aug 1998

Table 3. UMi-WFPC2 datasets: PSF photometry parameter values

Chip	Filter	$\chi$	Sharpness	Aperture Correction	Zero-pt Difference
WF2	F606W	1.70	0.50	1.24	−0.058
	F814W	1.60	0.50	1.29	−0.046
WF3	F606W	1.80	0.50	1.27	−0.038
	F814W	2.20	0.60	1.34	−0.013
WF4	F606W	1.70	0.50	1.27	−0.048
	F814W	1.65	0.50	1.33	+0.020

Note. — The third and fourth columns are the maximum values of the  $\chi$  and sharpness parameters for a detection to be accepted as stellar, the fifth column is the (multiplicative) aperture correction to a 0.5'' aperture, while the sixth column gives the zero-point difference between the psf photometry and the aperture photometry, in the sense ‘psf–ap’.

Table 4. WFPC2 Photometry of Unresolved Objects in the UMi-Off Field

$V_{606}$	$I_{814}$	$V_{606}-I_{814}$
22.37	20.07	2.30
23.14	20.38	2.77
23.93	21.41	2.52
25.01	24.15	0.86
25.11	23.41	1.70
25.44	24.62	0.82
25.52	24.45	1.05
25.66	24.38	1.28
25.76	23.32	2.44
25.78	25.03	0.75
25.83	22.75	3.08
25.88	25.71	0.18
26.05	25.92	0.13
26.21	24.37	1.84
26.74	23.21	3.50
26.76	26.22	0.54
26.78	26.12	0.65
27.01	25.93	1.08
27.51	26.58	0.92
27.70	26.83	0.88
27.76	27.13	0.58

Table 5. The  $V_{606}$  Counts and Completeness Function of the UMi dSph.

$V_{606}$	Star Counts			Completeness Functions		
	WF2	WF3	WF4	WF2	WF3	WF4
21.25	5	1	2	1.	1.	1.
21.75	2	2	1	1.	1.	1.
22.25	1	5	10	1.	1.	1.
22.75	20	19	22	1.	1.	1.
23.25	29	20	16	1.	1.	1.
23.75	35	39	33	1.	1.	1.
24.25	47	47	45	1.	1.	1.
24.75	61	64	54	1.	1.	1.
25.25	58	90	59	1.	1.	1.
25.75	82	75	71	1.	1.	1.
26.25	106	98	96	1.	0.99	1.
26.75	107	100	101	0.99	0.97	0.99
27.25	186	185	149	0.96	0.93	0.97
27.75	316	260	243	0.85	0.79	0.88
28.25	340	274	308	0.58	0.53	0.60
28.75	388	309	324	0.23	0.13	0.20
29.25	227	152	151	0.04	0.01	0.01
29.75	27	5	11	<0.01	<0.01	<0.01

Table 6. The  $I_{814}$  Counts and Completeness Function of the UMi dSph.

$I_{814}$	Star Counts			Completeness Functions		
	WF2	WF3	WF4	WF2	WF3	WF4
20.25	1	1	2	1.	1.	1.
20.75	6	2	2	1.	1.	1.
21.25	1	2	4	1.	1.	1.
21.75	3	5	4	1.	1.	1.
22.25	20	16	21	1.	1.	1.
22.75	27	24	19	1.	1.	1.
23.25	39	42	31	1.	1.	1.
23.75	49	50	52	1.	1.	1.
24.25	65	80	63	1.	1.	1.
24.75	74	90	64	1.	1.	1.
25.25	105	108	103	1.	1.	1.
25.75	122	133	119	1.	1.	1.
26.25	187	197	137	0.98	0.95	0.98
26.75	295	255	248	0.88	0.80	0.82
27.25	356	316	268	0.50	0.40	0.39
27.75	391	289	334	0.10	0.04	0.01
28.25	257	128	205	0.01	0.01	<0.01
28.75	39	8	21	<0.01	<0.01	<0.01

Table 7. The  $I_{LP}$  Luminosity Function of M15

$I_{LP,0}$	N	CF	LF
18.75	1	100.0	1.0
19.25	3	100.0	3.0
19.75	8	100.0	8.0
20.25	12	99.7	12.0
20.75	9	99.1	9.0
21.25	6	99.3	6.0
21.75	26	99.1	26.2
22.25	29	98.4	29.5
22.75	32	98.0	32.6
23.25	43	96.8	44.4
23.75	57	96.3	59.2
24.25	83	95.5	86.9
24.75	136	94.3	144.2
25.25	133	91.7	145.0
25.75	122	86.4	141.2
26.25	79	72.4	109.2
26.75	41	37.0	110.7
27.25	20	5.8	342.8

Table 8. The  $I_{LP}$  Luminosity Function of the Ursa Minor dSph.

$I_{LP,0}$	N	$N_{\text{off}}$	CF	LF
23.25	1	0	99.6	1.0
23.75	6	0	99.6	6.0
24.25	6	0	99.6	6.0
24.75	25	0	98.6	25.4
25.25	20	0	97.9	20.4
25.75	21	0	97.0	21.7
26.25	17	1	96.6	16.6
26.75	32	1	93.2	33.2
27.25	41	1	91.4	43.8
27.75	58	5	83.9	63.2
28.25	70	18	76.3	68.1
28.75	69	14	58.3	94.4
29.25	38	4	21.2	160.4
29.75	13	1	1.9	639.8

Table 9. The Selected WFPC2 Luminosity Functions of the UMi dSph.

$V_{606}$	LF	$I_{814}$	LF
23.25	64	22.25	57
23.75	107	22.75	61
24.25	139	23.25	110
24.75	172	23.75	149
25.25	201	24.25	201
25.75	215	24.75	218
26.25	270	25.25	294
26.75	257	25.75	323
27.25	433	26.25	477
27.75	786	26.75	860
28.25	1391	27.25	(1978)
28.75	(5408)	27.75	(38100)
29.25	(35880)	28.25	(47800)

Fig. 1.— Final drizzled WFPC2  $V_{606}$  image of the Ursa Minor field.

Fig. 2.— Final drizzled WFPC2  $V_{606}$  image of the UMi offset field.

Fig. 3.— Example of cuts employed in the psf goodness-of-fit statistics to reject resolved objects, cosmic rays, etc. (see also Table 3) for the WF4 F814W image of the Ursa Minor dSph field. Detections having  $\chi$  and/or sharpness values placing them above the dashed lines in this figure were rejected.

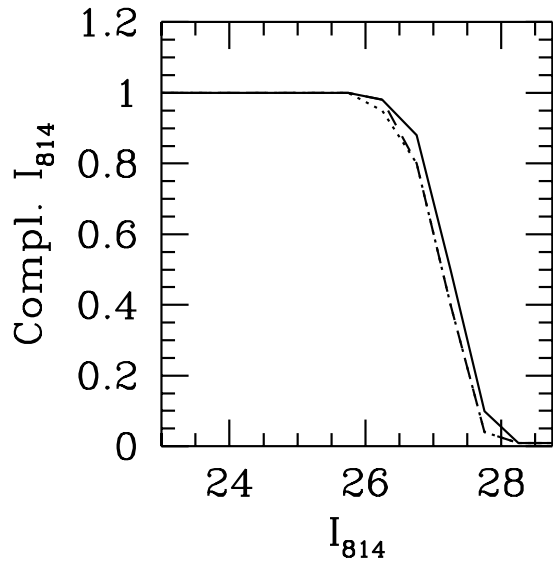
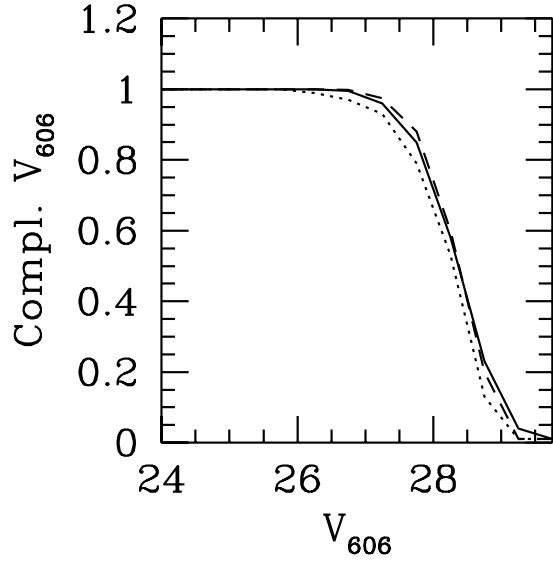


Fig. 4.— Completeness as a function of calibrated magnitudes,  $V_{606}$  and  $I_{814}$ . Full lines are completeness functions derived for WF2, dotted lines for WF3, and dashed lines for WF4.

Fig. 5.— The drizzled STIS LP image of our field in the UMi dSph galaxy.

Fig. 6.— The drizzled STIS LP image of our offset field lying  $\sim 2.5$  tidal radii from the centre of the UMi dSph galaxy, along the minor axis.

Fig. 7.— The  $\chi$  and sharpness values of objects detected on the M15 STIS LP image. The horizontal dotted lines show the values these parameters would assume for objects that are perfectly fit by the psf; the dashed lines show the boundary values that we adopted for detected objects to be classified as stars (see text).

Fig. 8.— The  $\chi$  and sharpness values of objects detected on the UMi STIS LP image. The horizontal lines have the same meaning as in Fig. 7.

Fig. 9.— The  $\chi$  and sharpness values of objects detected on the image that results from  $2 \times 2$  binning of the post-CALSTIS M15 image. The overall  $\chi$  and sharpness distributions differ from those of the unbinned image (Fig. 7) but are very similar to those of the (on-chip) binned UMi-STIS data (Fig. 8). The dotted lines have the same meaning as in Fig. 7.

Fig. 10.— The upper panel shows the excellent correlation between the magnitude measured for a given object from the unbinned M15 data and the magnitude for the same object measured from the binned M15 data. The lower panel plots the differences between the binned and unbinned M15 magnitudes as a function of magnitude.

Fig. 11.— The  $\chi$  and sharpness values of objects detected on the UMi-off-STIS image. The left-hand panels show the psf-fitting statistics when the psf derived from the single bright star in the UMi-off-STIS image is used for the photometry; the right-hand panels show the psf-fitting statistics when the psf derived from the drizzled UMi STIS-LP image is used instead. The horizontal lines have been taken directly from Fig. 7.

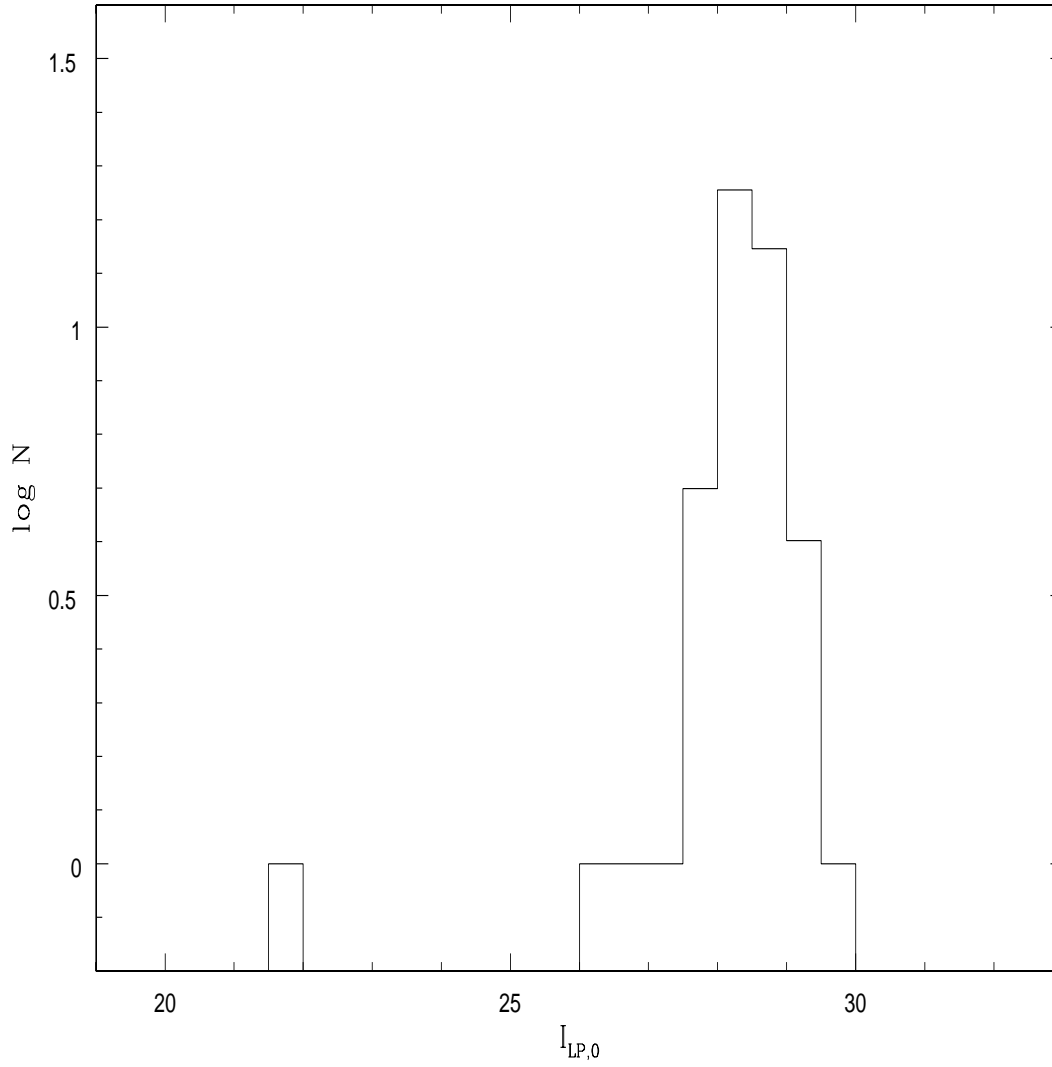


Fig. 12.— The luminosity function of objects detected in the UMi-off-STIS image, using the psf derived from that image, with the  $\chi$  and sharpness criteria set from the UMi-STIS image. As discussed in the text, these objects are likely to be just spurious detections.

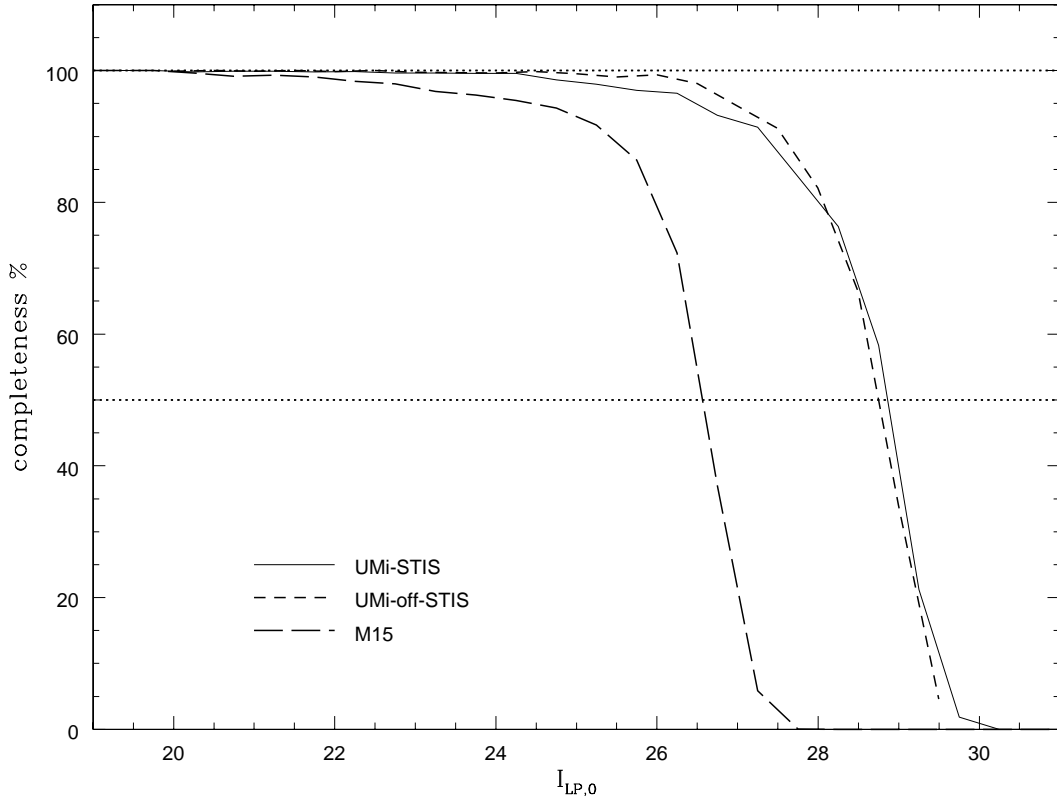


Fig. 13.— The completeness functions of the STIS data derived from the UMi-STIS image (solid curve) and the UMi-off-STIS image (short-dashed curve), both using the UMi-STIS psf. The good agreement shows that crowding is not an issue in the derivation of the completeness functions. The completeness function of the M15 data is also shown (long-dashed line). The UMi-off-STIS completeness function has been adjusted for the difference in the exposure times of the UMi-STIS and UMi-off-STIS images.

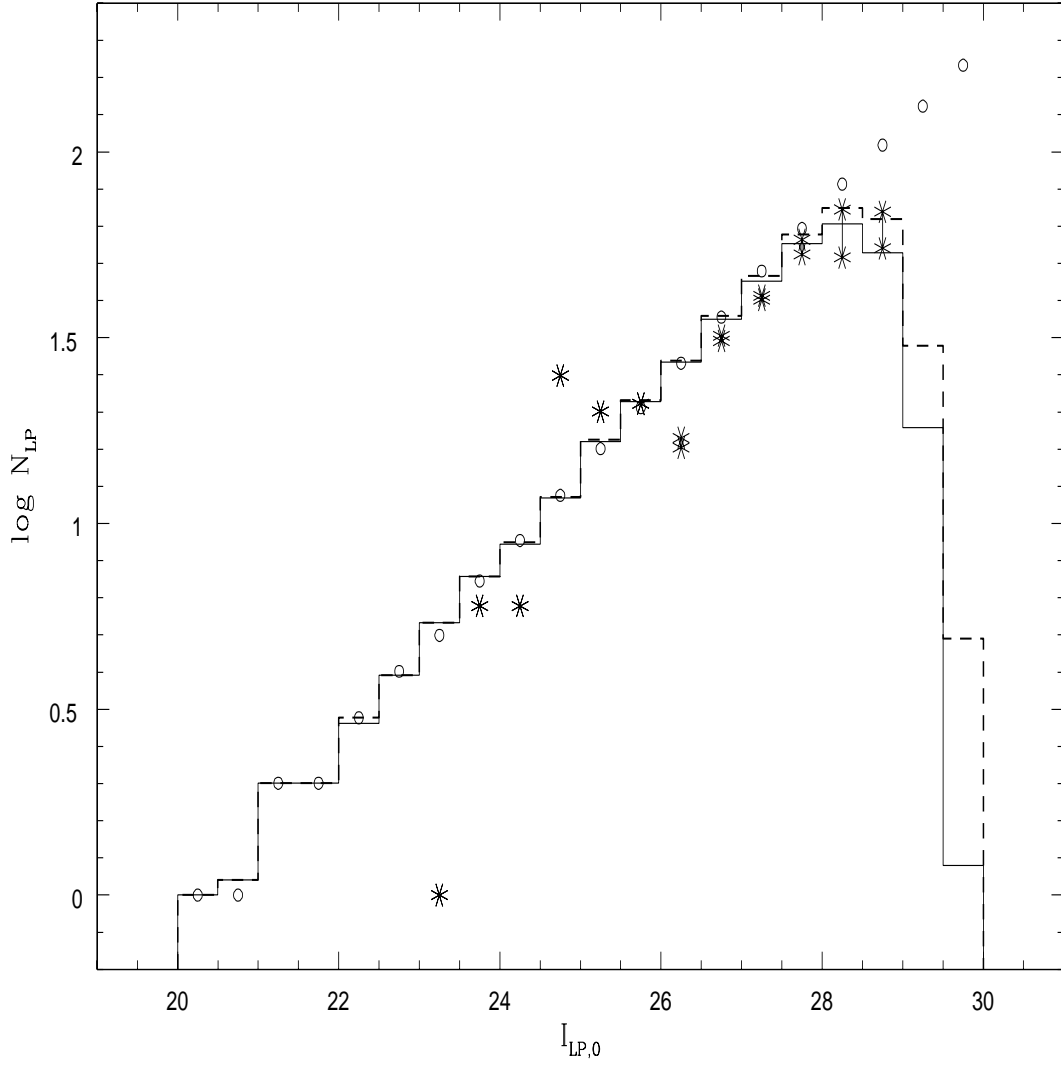


Fig. 14.— The solid histogram shows the luminosity function of artificial stars detected, and meeting the psf selection criteria, when the input magnitudes of the artificial stars (open points) are distributed in a power law that approximates the observed, completeness-corrected luminosity function of M15. The dashed lines shows all detected artificial stars (i.e. before psf selection criteria are considered). The observed (not completeness-corrected) luminosity function of the UMi dSph (asterisks), either with or without subtraction of off-field counts estimated as in the text (the range shown by connected asterisks), closely follows that of the recovered artificial stars.

Fig. 15.— The NIC2 F160W image of M15.

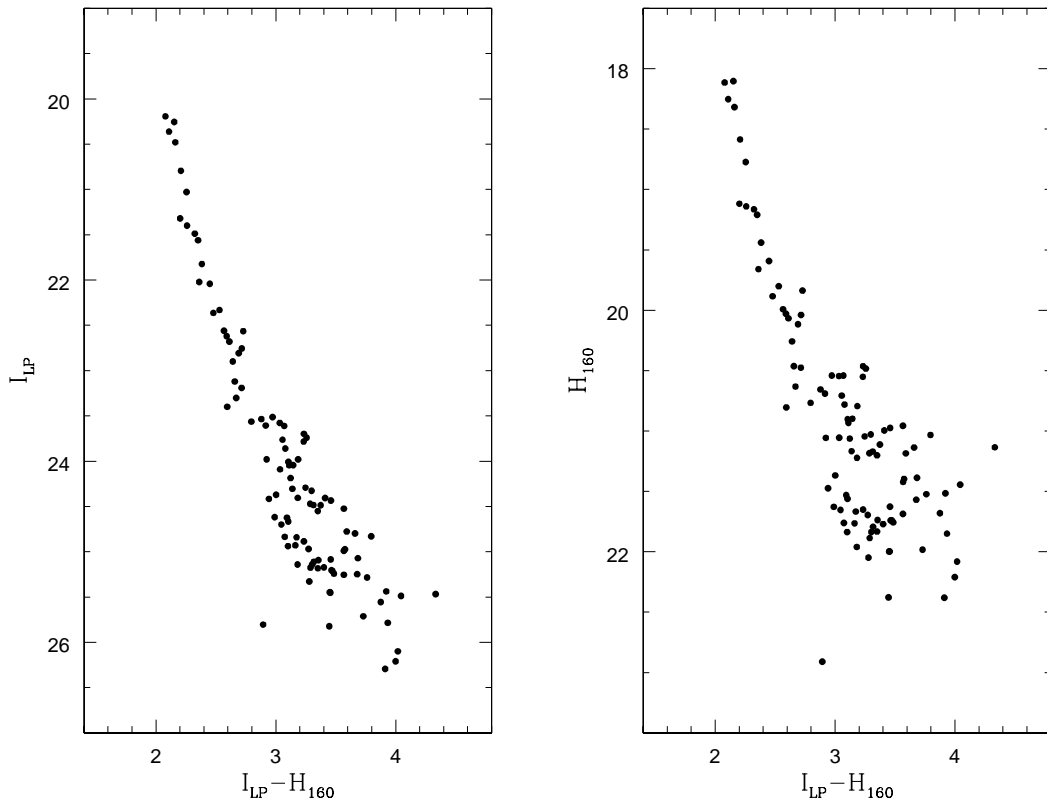


Fig. 16.— Color-magnitude diagrams of the stars detected in our STIS LP and NIC2 F160W images of M15.

Fig. 17.— The NIC1 F140W image of the Ursa Minor dSph.

Fig. 18.— The NIC2 F160W image of the Ursa Minor dSph.

Fig. 19.— Colour-magnitude diagrams for all three WF chips separately, plus the sum (clockwise from top left: WF2, WF3, WF4, sum).

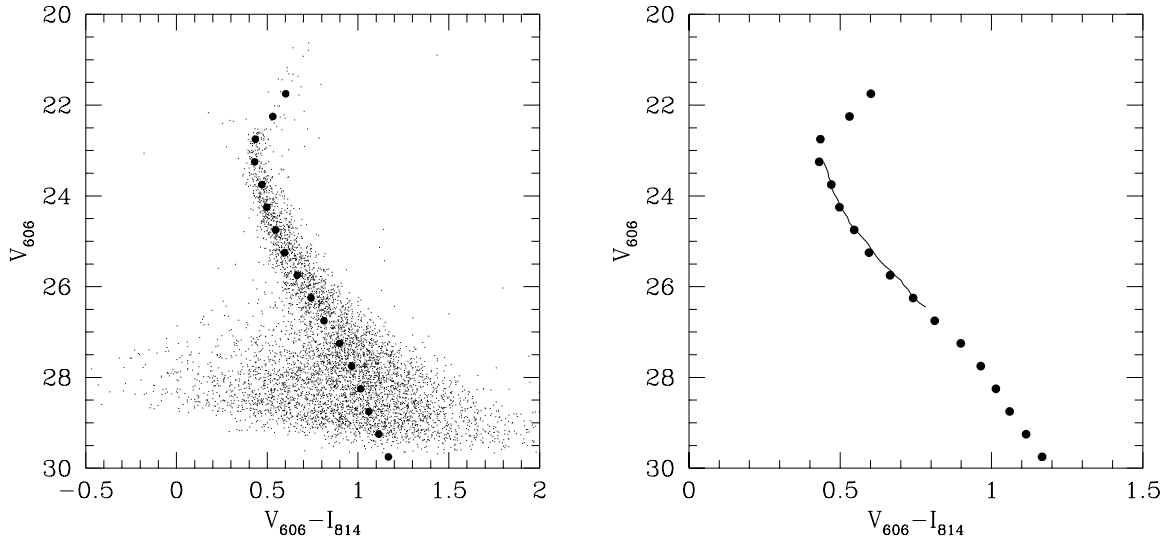


Fig. 20.— Left-hand panel: Comparison of the CMD for the Ursa Minor dSph with the ridge line we derived for M92 using data from Piotto et al. 1997 (filled circles), moved to the same distance modulus as the UMi dSph,  $m - M = 19.1$ . Right-hand panel: Comparison of the fiducial ridge line derived from our UMi data (continuous line; spline fit) with the fiducial for M92 (filled circles).

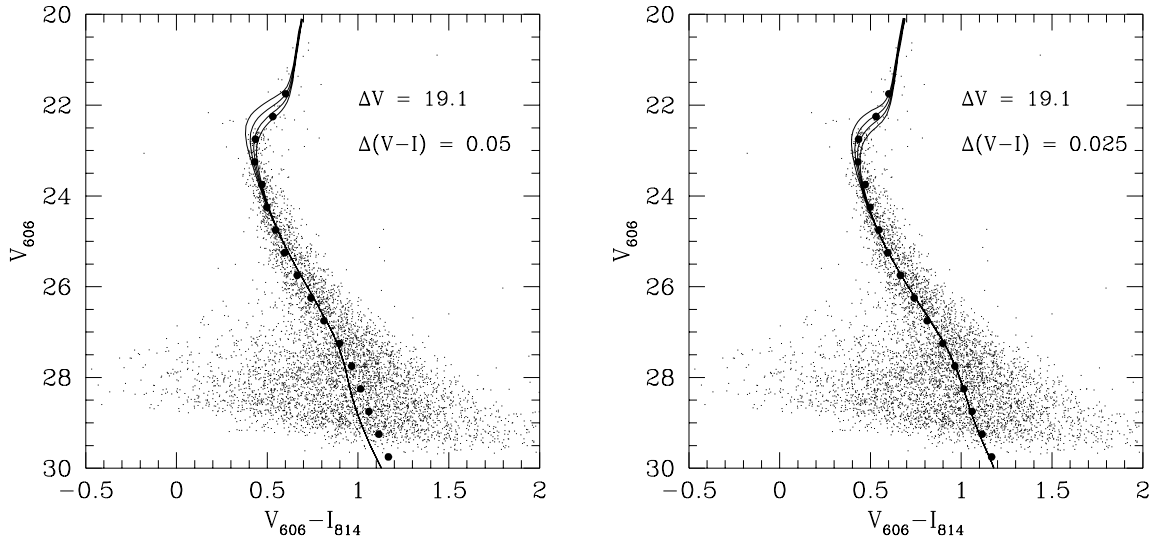


Fig. 21.— The CMD of the UMi dSph with superposed ridge line for M92 and isochrones from the Vandenberg & Bell (1985) models for ages of 12, 14, 16 and 18 Gyr and metallicities of  $-2.2$  dex (left-hand panel) and  $-1.5$  dex (right-hand panel). The isochrones have been shifted by the amounts indicated in the figures.

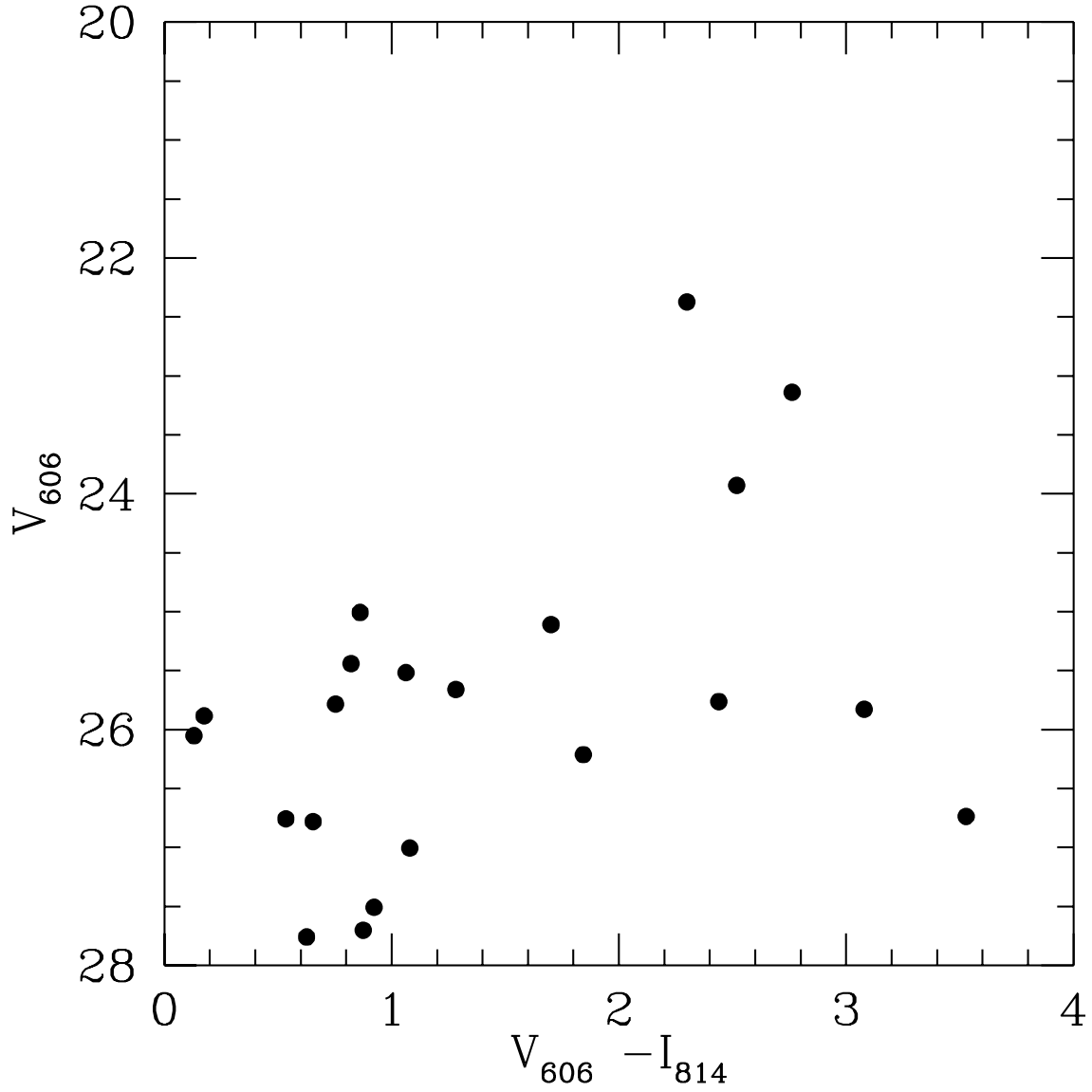


Fig. 22.— Colour-magnitude diagram for the unresolved objects meeting the  $\chi$  and sharpness criteria in the UMi-off-WFPC2 field. Note the wide colour range of the x-axis.

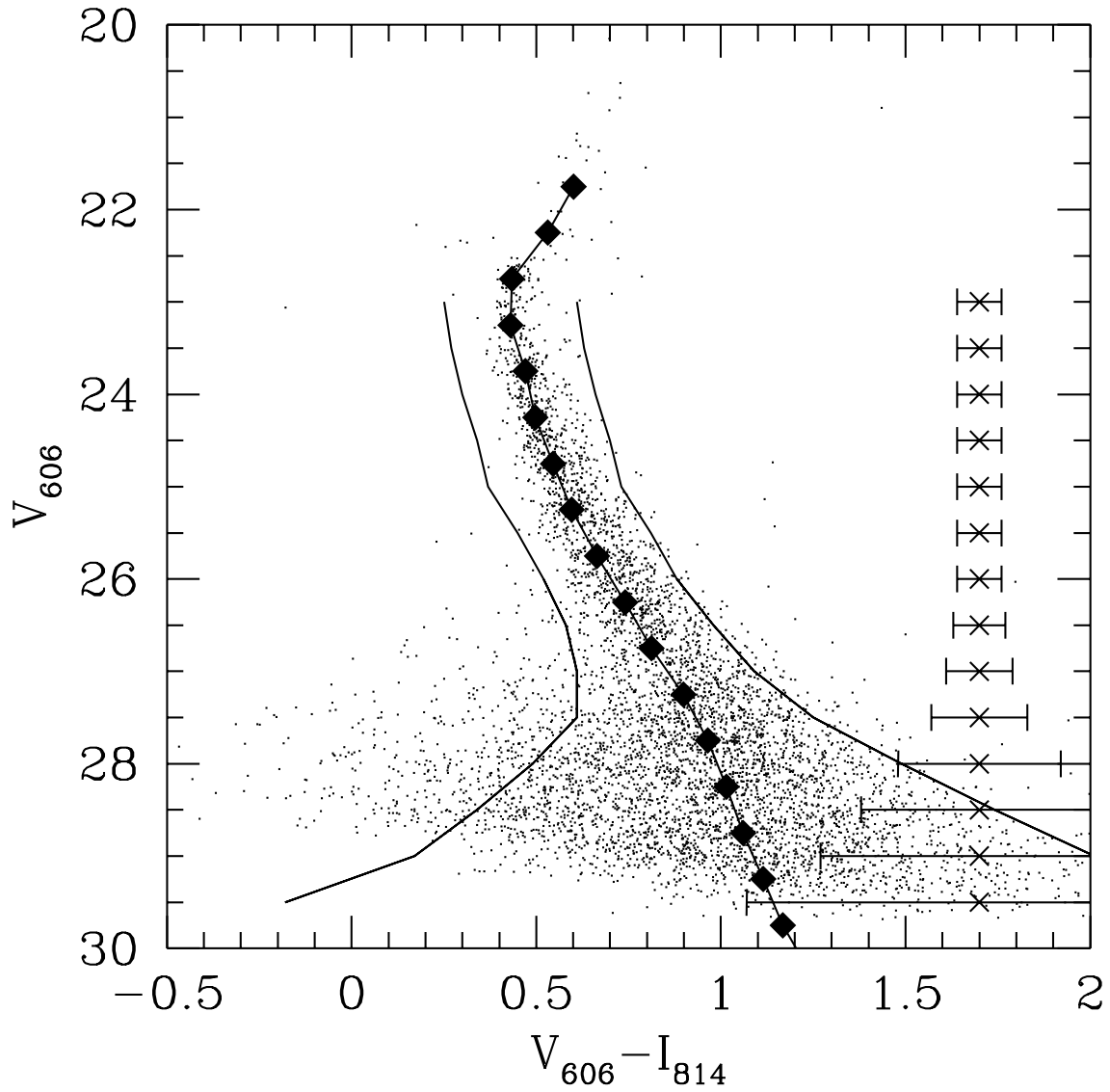


Fig. 23.— Colour-magnitude diagram for all three WFs. Full curves show the selection criteria for stars being included in the selected luminosity function.  $\times$  with error-bars (to the right) show typical errors for each magnitude bin.

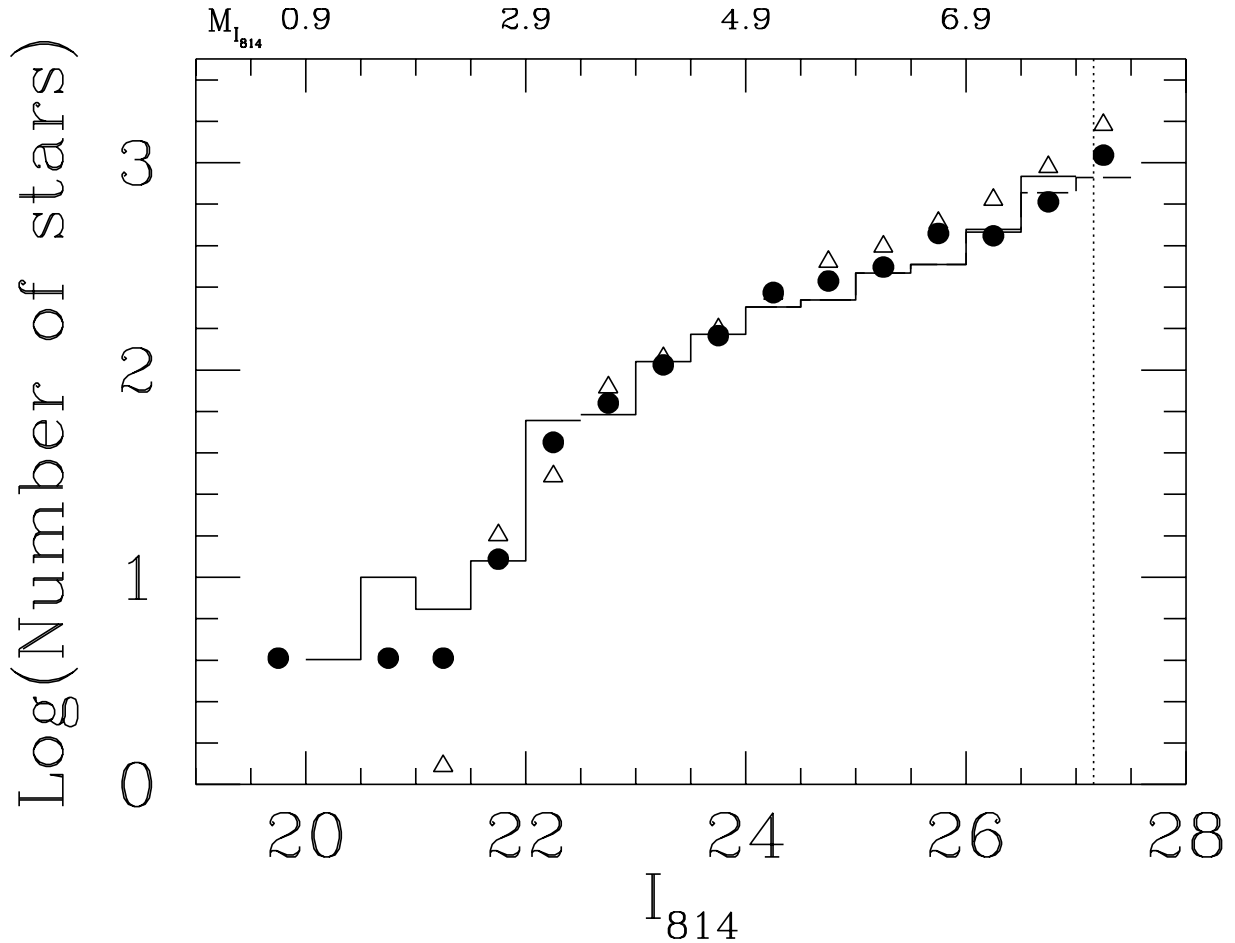


Fig. 24.—  $I_{814}$  luminosity function of the Ursa Minor dSph compared to those of M92 (filled circles) and of M15 (open triangles). The dashed line is the UMi luminosity function derived on the basis of the selection criteria of Fig. 23, prior to completeness corrections. The full line includes completeness corrections, with the vertical dotted line indicating the 50% completeness limit. The globular cluster data (Piotto et al. 1997) have been moved to the same distance modulus as the Ursa Minor dSph and normalized to the UMi counts as discussed in the text. The absolute magnitude is given along the upper x-axis.

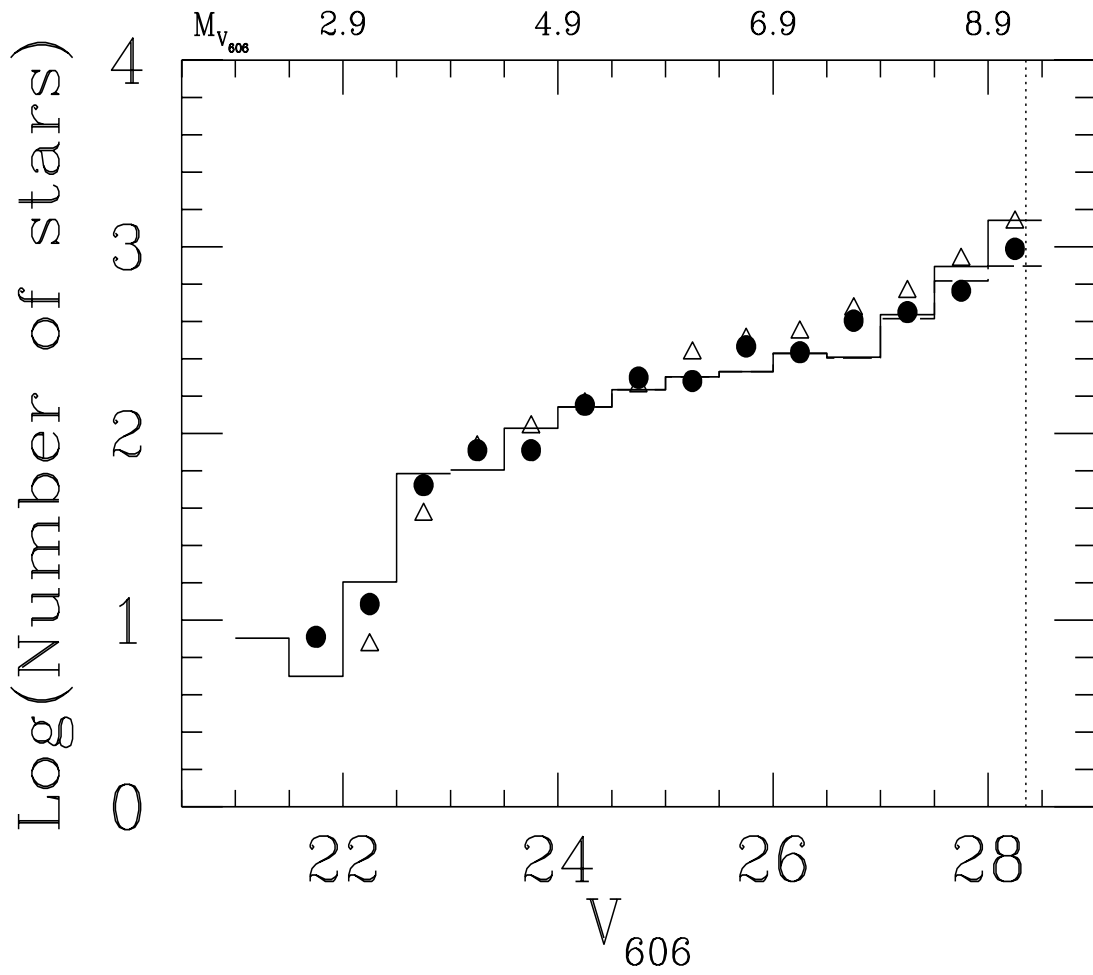


Fig. 25.— As Fig. 24 but for the data in the WFPC2 F606W filter.

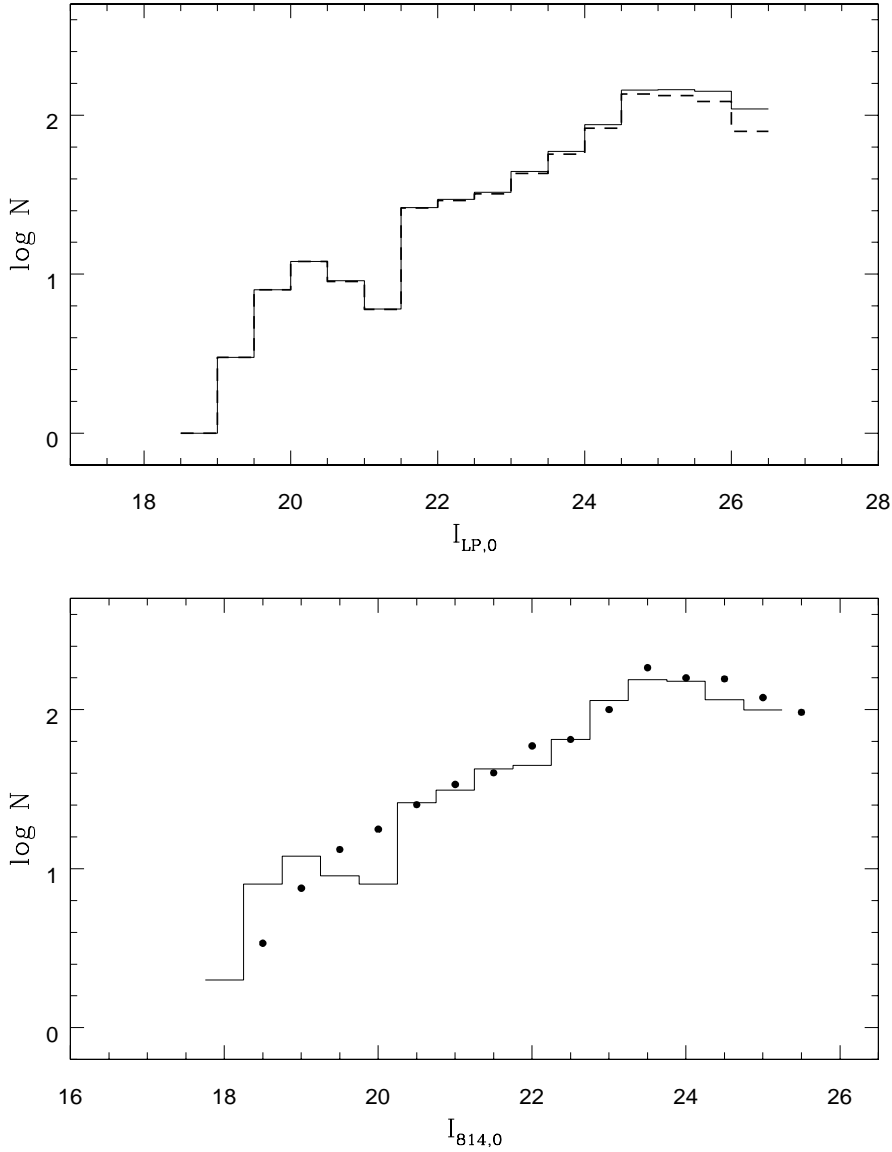


Fig. 26.— The luminosity functions of M15. Top panel: the raw (dashed line) and completeness-corrected (solid line) STIS LP luminosity functions of M15. Bottom panel: the WFPC2  $I_{814}$  luminosity function of M15 obtained (a) by transformation of the  $I_{LP}$  luminosity function (solid line) and (b) by Piotto, Cool, & King (1997) from their WFPC2 observations (points). These luminosity functions have been normalized to the STIS counts in the magnitude range  $20.5 \leq I_{814,0} \leq 23.0$ , and only those LF bins having completeness levels greater than 50% are plotted. The actual WFPC2 counts are larger, scaling as the field-of-view, resulting in the smoothing-out of low-statistical significance features in the STIS-based luminosity function, such as the deficit at  $I_{814,0} = 20$ .

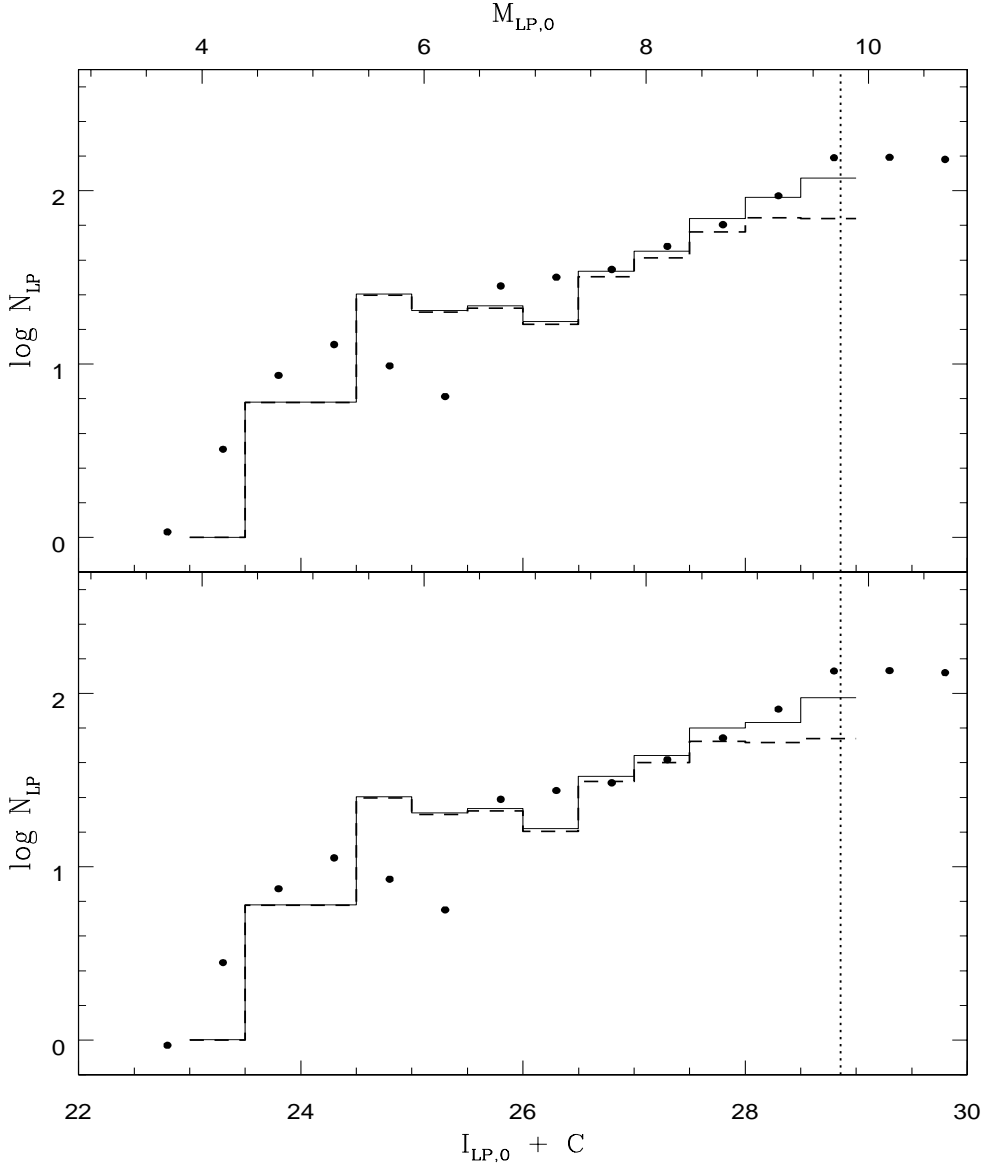


Fig. 27.— The STIS  $I_{LP}$  luminosity functions of the UMi dSph galaxy. The top panel shows the luminosity functions without any correction for the counts in the offset field, while the lower panel shows the luminosity functions after subtracting the counts in the offset field. The raw (dashed line) and completeness-corrected (solid line) STIS luminosity functions of UMi are compared to the completeness-corrected luminosity function of M15 (points; shifted by 4 magnitudes to match the reddening-corrected distance modulus of the UMi dSph). The UMi and M15 LFs in each panel have been normalized in the magnitude range  $26.5 \leq I_{LP,0} \leq 28.5$ , and only the LF bins that are more than 50% complete are plotted. The absolute magnitudes are shown along the upper x-axis.

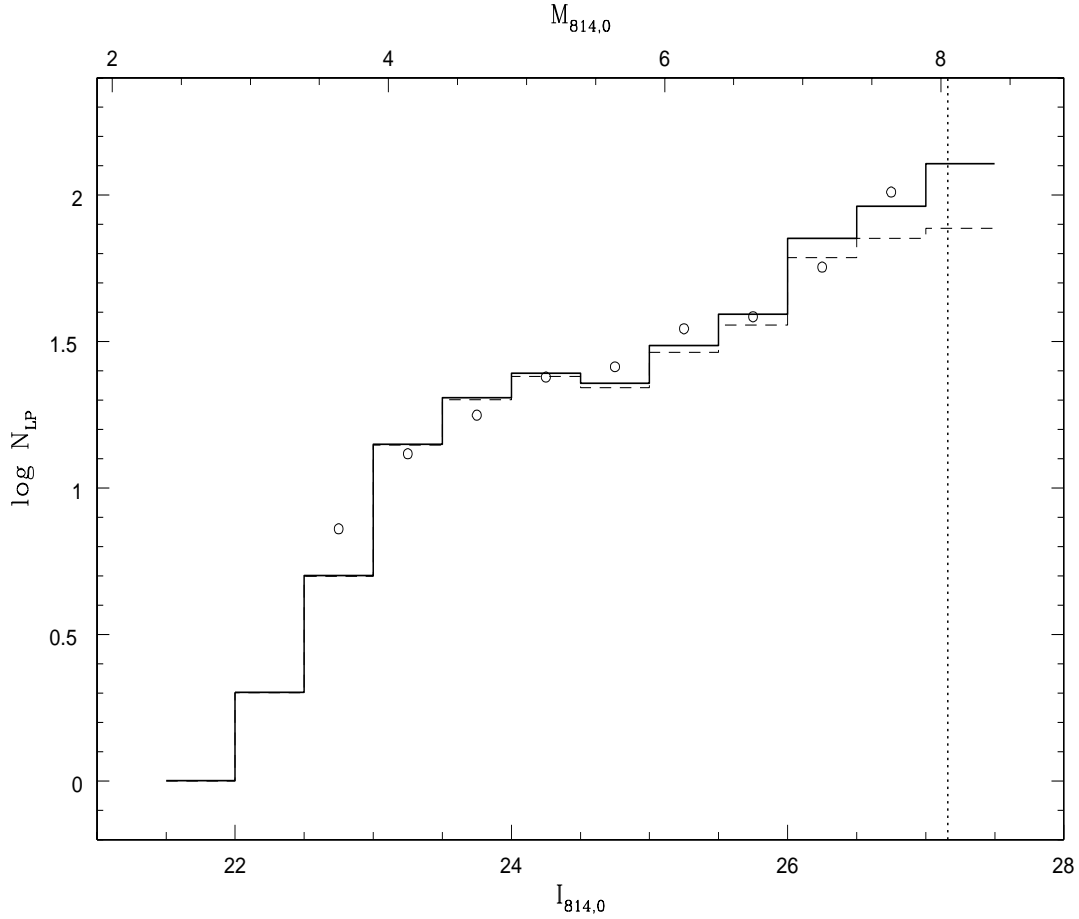


Fig. 28.— The transformed (from  $I_{LP}$ )  $I_{814}$  luminosity functions for the UMi dSph (dashed histogram represents the raw counts, the solid histogram is completeness-corrected) are compared to the directly observed  $I_{814}$  luminosity function of the UMi dSph (open points). The LFs are normalized in the magnitude range  $25 \leq I_{814,0} \leq 27$ , and only the LF bins which are more than 50% complete are plotted; there is clearly excellent agreement between these two independent measures of the I-band luminosity function.

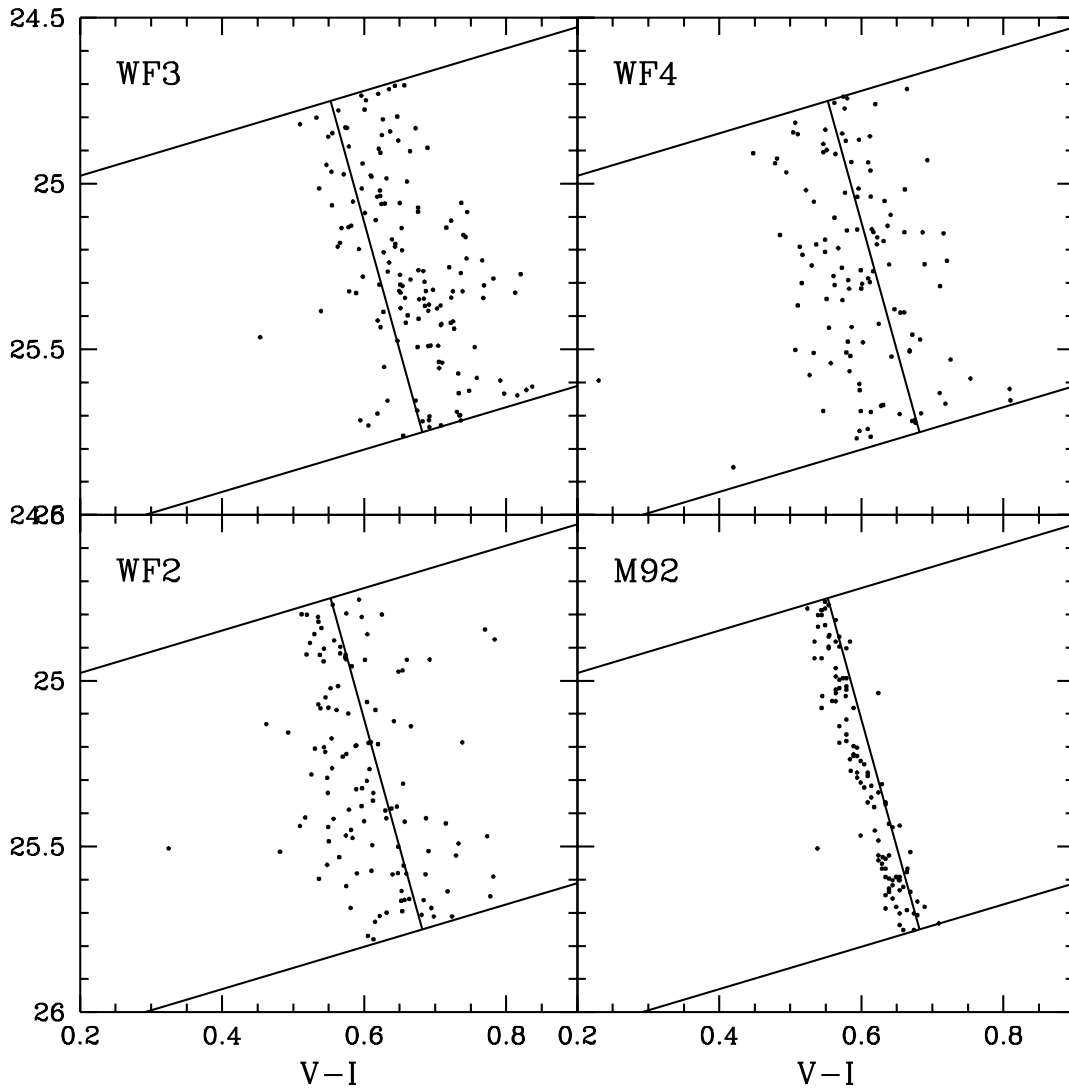


Fig. 29.— The fiducial ridge for the Ursa Minor dSph overlaid on the UMi upper main sequences from each of the three WF chips, plus that for M92 (moved to the same distance modulus as UMi).

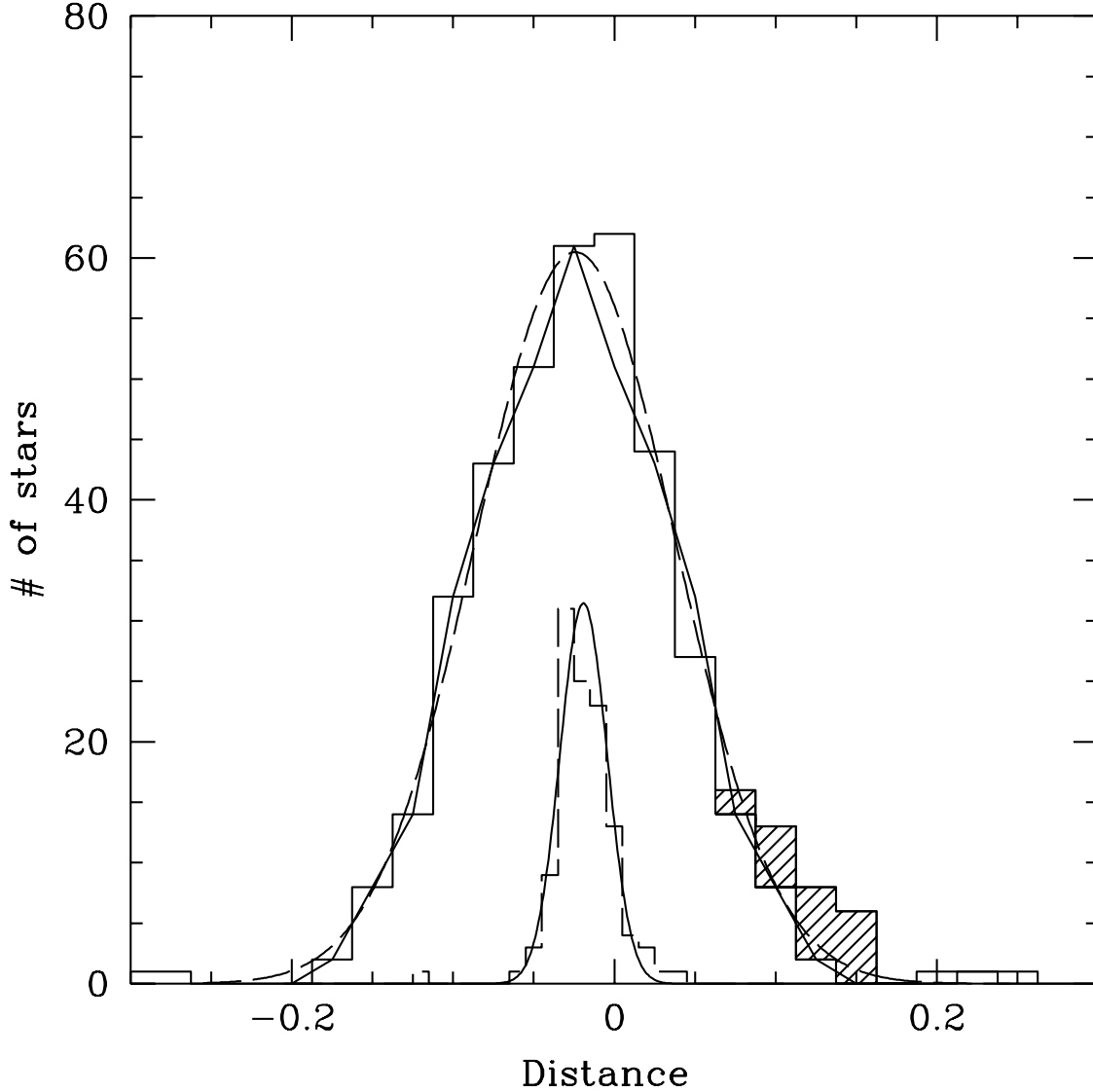


Fig. 30.— The large full histogram represents the distribution of the perpendicular distances from the fiducial ridge line of stars in the selected upper main sequence region of the Ursa Minor CMD, constructed as described in the text. The smaller dashed histogram results from the same analysis applied to M92 (using the Ursa Minor fiducial, with M92 moved to the same distance modulus). The Gaussians superposed (dashed curve for the Ursa Minor data, continuous curve for the M92 data) have  $\sigma$  set equal to the typical errors (0.043 for the Ursa Minor data and 0.015 for the M92 data). For the Ursa Minor data, we also show the distribution that results when the blue half of the histogram is mirrored to the red side; this is indicated by the continuous curve. The shaded area shows the red excess, signalling the presence of unresolved binaries.

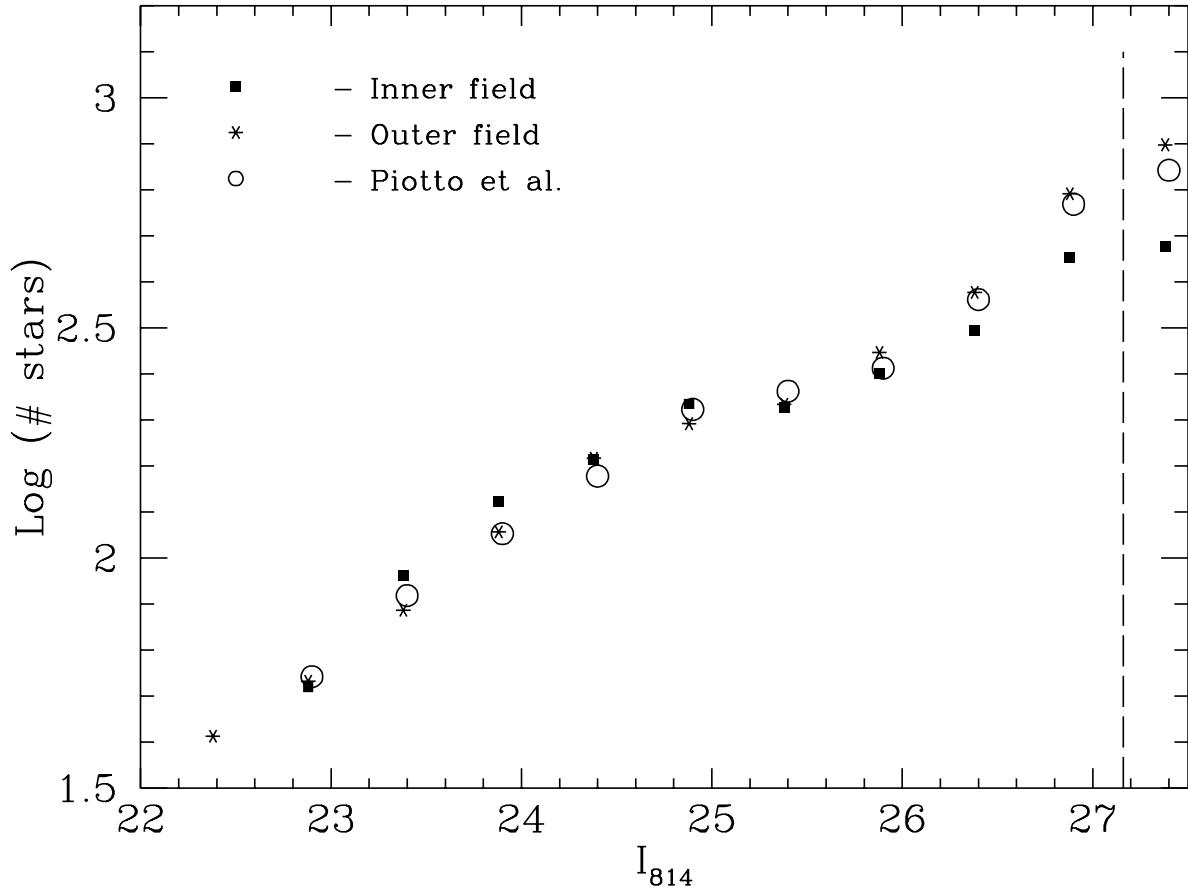


Fig. 31.— Comparison between the luminosity function measured at different projected radii in M92. The inner and outer fields from Andreuzzi et al. (2000) are situated at 13 and 21 core radii, respectively, while the Piotto et al. (1997) field is at 22 core radii. The data have been shifted to match the distance modulus of the Ursa Minor dSph and are normalized at  $25 < I_{814} < 26$ . The dashed vertical line denotes the equivalent 50% completeness of our Ursa Minor data.

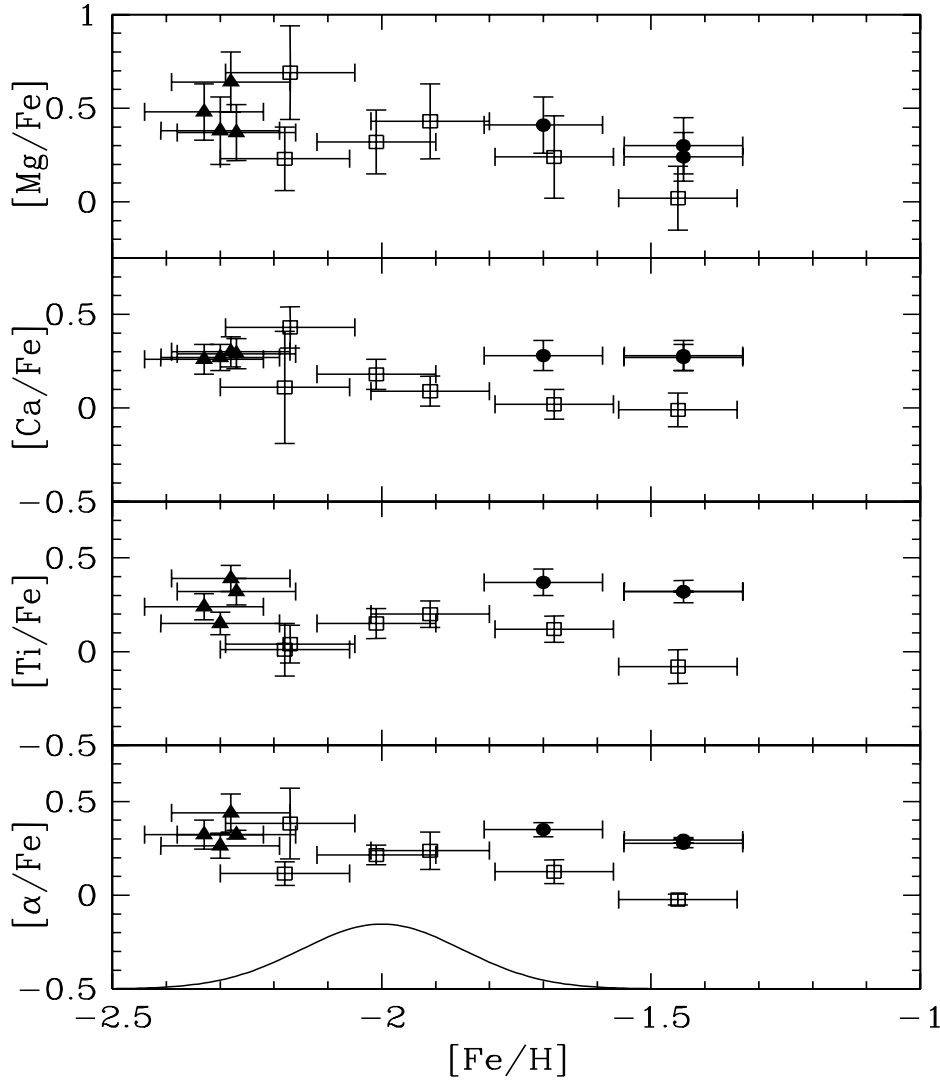


Fig. 32.— Comparison of the elemental abundances measured by Shetrone, Côté & Sargent (2001) for stars in the globular clusters M92 (filled triangles) and M3 (filled circles), and in the dwarf spheroidal in Ursa Minor (open squares). The quantity in the lowest panel is just the mean of the elemental ratios in the upper three panels, and following Shetrone et al. the error bars have been correspondingly reduced, assuming three independent measurements. The smooth Gaussian indicates the intrinsic metallicity distribution of the UMi dSph. Most of the stars in the UMi dSph, represented by the 4 metal-poor member stars here,  $[Fe/H] \lesssim -2$  dex, have elemental abundances consistent with those of the member stars in the globular clusters, indicative of Type II supernova enrichment. The more metal-rich stars in this system are consistent with forming from more iron-enriched gas, indicative of enrichment by Type Ia supernovae. This pattern is as expected from the star formation history inferred from the colour-magnitude diagram, but awaits confirmation from larger samples of UMi stars with fine abundance analyses.

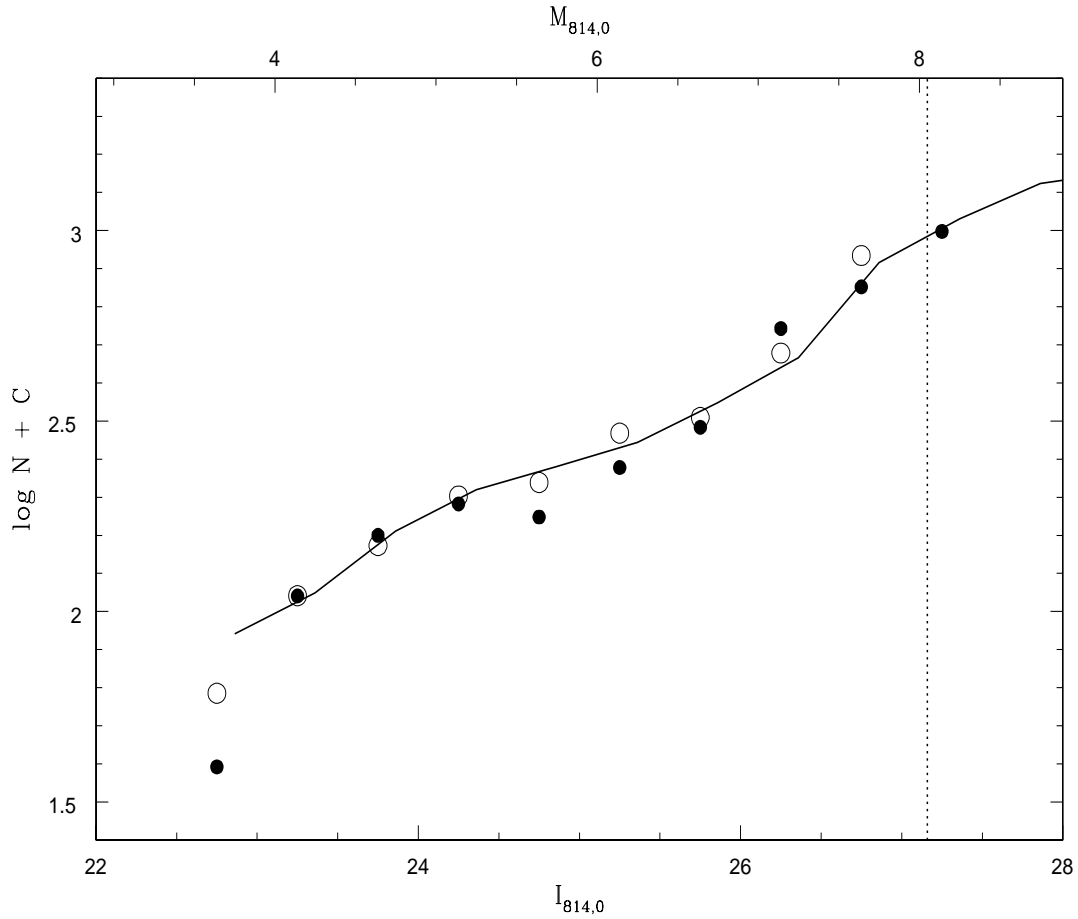


Fig. 33.— The I-band luminosity function for the UMi dSph (solid points, transformed from  $I_{LP}$ ; open points WFPC2 data). Only bins greater than 50% complete are shown, and the dotted vertical line indicates the 50% completeness of the WFPC2 data. The solid line shows the predicted luminosity function for a low-mass mass function of slope  $-1.8$ , based on the Baraffe et al. (1997) models.

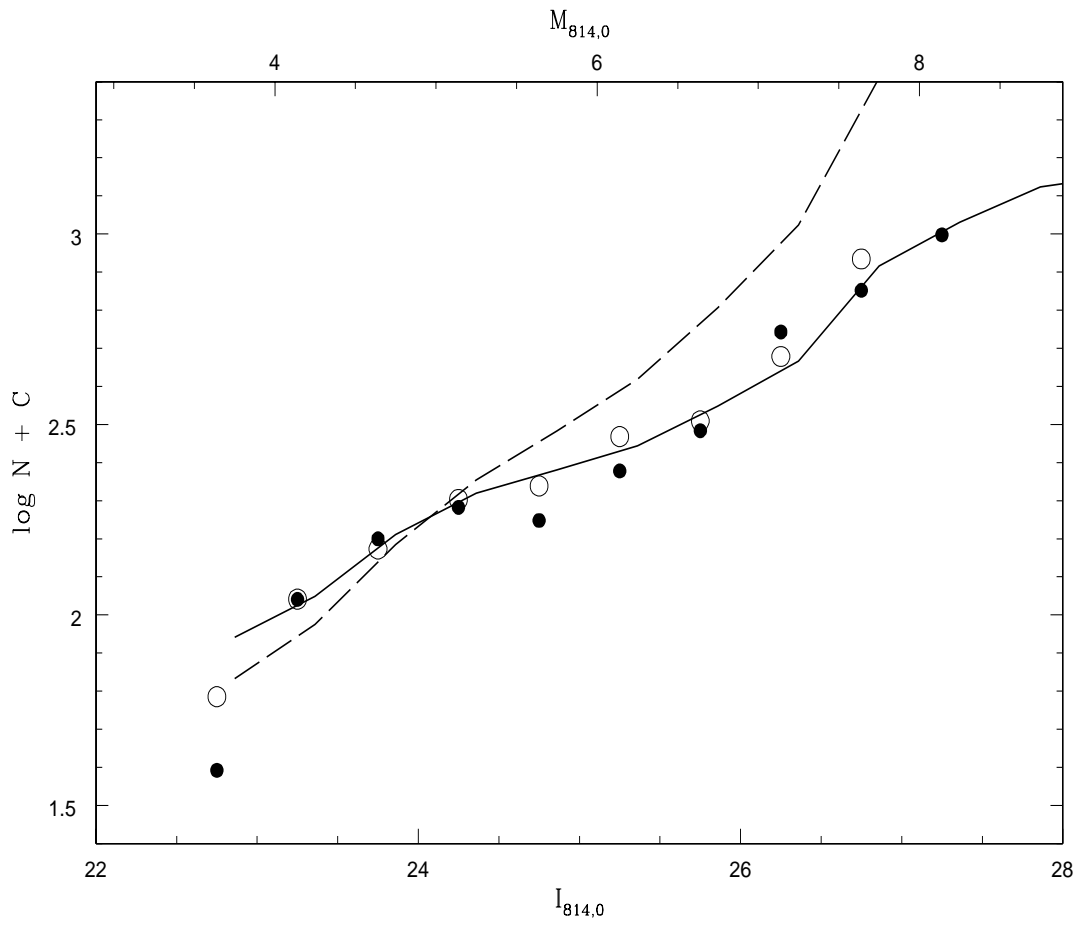


Fig. 34.— As Fig. 33, but with the addition of the predictions of a mass function slope of  $-3.66$  (dashed line). The observations clearly do not favour this steeper mass function.

This figure "fig1.jpg" is available in "jpg" format from:

<http://arxiv.org/ps/astro-ph/0206144v1>

This figure "fig2.jpg" is available in "jpg" format from:

<http://arxiv.org/ps/astro-ph/0206144v1>

This figure "fig3.jpg" is available in "jpg" format from:

<http://arxiv.org/ps/astro-ph/0206144v1>

This figure "fig5.jpg" is available in "jpg" format from:

<http://arxiv.org/ps/astro-ph/0206144v1>

This figure "fig6.jpg" is available in "jpg" format from:

<http://arxiv.org/ps/astro-ph/0206144v1>

This figure "fig7.jpg" is available in "jpg" format from:

<http://arxiv.org/ps/astro-ph/0206144v1>

This figure "fig8.jpg" is available in "jpg" format from:

<http://arxiv.org/ps/astro-ph/0206144v1>

This figure "fig9.jpg" is available in "jpg" format from:

<http://arxiv.org/ps/astro-ph/0206144v1>

This figure "fig10.jpg" is available in "jpg" format from:

<http://arxiv.org/ps/astro-ph/0206144v1>

This figure "fig11.jpg" is available in "jpg" format from:

<http://arxiv.org/ps/astro-ph/0206144v1>

This figure "fig15.jpg" is available in "jpg" format from:

<http://arxiv.org/ps/astro-ph/0206144v1>

This figure "fig17.jpg" is available in "jpg" format from:

<http://arxiv.org/ps/astro-ph/0206144v1>

This figure "fig18.jpg" is available in "jpg" format from:

<http://arxiv.org/ps/astro-ph/0206144v1>

This figure "fig19.jpg" is available in "jpg" format from:

<http://arxiv.org/ps/astro-ph/0206144v1>